Numerical Simulation of Low-Pressure Turbine Blade Separation Control

A. Gross* and H. F. Fasel[†]

University of Arizona, Tucson, Arizona 85721

Low-pressure turbines are a common and important element of many modern jet engines. Any performance improvement will lead to net savings in aircraft operating costs. At low operating Reynolds numbers or for reduced stage solidities laminar separation from the constituent blades can noticeably deteriorate overall engine performance. Under such conditions active control of laminar separation may eliminate or reduce associated losses resulting in increased engine performance. A high-order-accurate finite volume Navier–Stokes code for investigating separation control for the PackB blade geometry at a Reynolds number based on axial chord of 25,000 was employed. For this Reynolds number laminar separation was observed in the experiments. First, a grid resolution study for the uncontrolled flow was carried out, which shows grid convergence for our simulations. Then separation control by pulsed vortex generator jets was investigated. It is shown how this control results in an earlier transitioning of the flow and the introduction of spanwise coherent structures. The increased wall-normal mixing associated with these two mechanisms results in an effective separation control. An even more efficient separation control can be accomplished by harmonic blowing through a slot. The astounding effectiveness of the latter control scheme is attributed to an amplification of the disturbance input through a hydrodynamic instability mechanism and to the suppression of three-dimensional structures, which weaken the spanwise structures. Finally, separation control by streamwise vortices that were generated by volume forces was investigated. As the flow does not amplify such structures the energy input required for accomplishing an effective control was found to be large compared with the other flow control techniques. Because the structures are steady they can, however, likely be generated with passive devices such as vortex generators.

Nomenclature

a	=	proper orthogonal decomposition time coefficient, ellipse semiaxis, Fourier coefficient
A	=	volume force, mode amplitude
B	=	blowing ratio
b	=	slot width, ellipse semiaxis
C_x	=	axial chord length
C_s	=	suction side arclength
$\mathbf{C}$	=	correlation tensor
c	=	Fourier coefficient
c_f	=	skin friction coefficient
c_p	=	pressure coefficient
c_μ	=	momentum coefficient
d	=	blade spacing, distance to trailing edge
E	=	energy spectral density estimate
f	=	frequency, volume force
K	=	number of cells in spanwise direction
k	=	spanwise mode number, turbulence kinetic energy, number of streamwise vortices
L_k	=	Kolmogorov length scale
l	=	cell index in spanwise direction
N	=	number of timesteps
n	=	wall-normal coordinate, temporal mode, timestep
p	=	static pressure
Q	=	vortex identification criterion
$\mathbf{q}$	=	proper orthogonal decomposition mode
R	=	hole radius
r	=	radial coordinate, radius
$\mathbf{r}$	=	right eigenvector
S	=	strain rate tensor
s	=	arclength, strain rate tensor
t	=	time
T	=	period
u, v, w	=	velocity components
$\mathbf{v}$	=	velocity vector
u_τ	=	friction velocity
W	=	vorticity tensor
x, y, z	=	coordinates
$\mathbf{x}$	=	coordinate vector
ΔT	=	time interval
ΔZ	=	spanwise grid extent
δ	=	Kronecker symbol
ε	=	turbulence dissipation
ϑ	=	angular coordinate
λ	=	wavelength, eigenvalue
μ	=	dynamic viscosity
ν	=	kinematic viscosity
ρ	=	density
τ	=	duty cycle
Ψ	=	streamfunction
ω	=	vorticity

Subscripts

c	=	cosine
f	=	forcing
i	=	proper orthogonal decomposition mode number
i, j, l	=	coordinate indices
in	=	inlet conditions
max	=	maximum
n	=	Fourier mode number
r	=	radial direction
s	=	sine

*Assistant Research Professor. Member AIAA.
[†]Professor. Member AIAA.

tot	=	total
wall	=	wall quantity
z	=	spanwise direction

Superscripts

+	=	in wall units
*	=	dimensional quantity
k	=	spanwise mode
n	=	temporal mode, timestep

I. Introduction

EFFORTS aimed at increasing the efficiency of jet engines demand that low-pressure turbines (LPTs) drive larger fans at lower speed. In parallel, attempts are made to decrease the stage solidity (inverse of the blade spacing) for reducing the engine weight. Both measures, especially when operating under low Reynolds number conditions (such as high altitude) or for small engine dimensions (which are typical for unmanned aerial vehicles), can lead to laminar separation which incurs significant turbine and overall engine performance losses. Separation occurs when the flow cannot negotiate the adverse pressure gradient associated with the pressure recovery in the aft part of the blade. Flow control techniques, both passive and active, that reduce or eliminate laminar separation would allow for the design of more efficient and more light weight engines. For example, active flow control (AFC) can be implemented to either prevent separation during nominal operation or to control separation during critical off-design phases. Active flow control techniques (such as vortex generator jets or plasma actuators) require energy but can be shut off when not needed. Passive flow control techniques (such as vortex generators or dimples) come free of charge but cause losses when not needed.

Earlier experiments at the U.S. Air Force Research Laboratory at Wright-Patterson Air Force Base with a linear cascade of PackB LPT blades have demonstrated convincingly that AFC by means of pulsed vortex generator jets (VGJs) can effectively control separation [1–3]. The PackB profile is a low Mach number scaled high performance blade originally released by Pratt and Whitney. For VGJ control, fluid is injected into the boundary layer through a spanwise array of small holes that are placed along the spanwise direction on the suction side of the blade upstream of the separation line. The stunning performance of pulsed versus steady VGJs was attributed to an earlier transitioning of the separated boundary layer that either resulted in a complete separation prevention or an earlier reattachment of the turbulent boundary layer. It was also found that, when compared with steady VGJs, the mass flow required for a successful separation control by pulsed VGJs was significantly lower. Simulations [4–11] and biglobal stability analysis results [12,13] suggest that the laminar separation bubble that typically arises in LPT applications is absolutely unstable in the natural uncontrolled case. The bubble oscillates in a self-excited fashion and sheds large spanwise coherent structures. In fact, it was found that the in-phase actuation of the VGJs introduces a 2D disturbance that experiences exponential growth indicating a linear instability of the flow [10]. By choosing proper VGJ actuation parameters this instability can be exploited and the required forcing amplitudes can be quite low. In this context the VGJ hole spacing is a particularly important parameter as it determines the initial amplitude of the 2D disturbance relative to the three-dimensional (3D) disturbance associated with the discrete hole spacing [9]. Harmonic blowing through a slot may be understood as the limiting case of pulsed VGJs with infinitely small hole spacing. In the experiment, a comparable disturbance input may be achieved with a plasma actuator. For example, experiments by Huang et al. demonstrated an effective separation control using plasma actuators [14]. Rizzetta and Visbal employed a high-order-accurate compressible Navier–Stokes code for investigating the fluid dynamics of separation control by pulsed VGJs [5] and plasma actuators [6]. Pulsed VGJs were found to result in an earlier transitioning of the suction side boundary layer. Pulsed plasma actuation was found to be

more effective than continuous operation. The effectiveness of the former was attributed to the generation of spanwise vortical structures (or spanwise *rollers*) that entrain high momentum fluid from the freestream.

Embacher performed an analysis of the secondary instability of the separation bubble and found that for certain frequencies of the primary wavy (spanwise rollers) the growth rates of secondary instability waves were reduced resulting in transition delay [15]. This concept was validated in a direct numerical simulation. Through the introduction of a 2D mode with a certain frequency (which was amplified by the flow but different from the natural shedding frequency) a laminar separation bubble with turbulent reattachment could be relaminarized. A similar effect could be observed in simulations of separation control by harmonic blowing through a slot for an LPT geometry [9]. The interaction of separation and transition [16] appears to play an important role in the context of LPT separation control.

We decided to investigate if similar effects could also be obtained through the forcing of streamwise vortices. Streamwise streaks have already been shown to stabilize Tollmien–Schlichting waves in the Blasius boundary layer [17]. From the onset of this investigation it was clear that the flow, because of the convex curvature on the suction side and despite the slight streamwise excess velocity near the wall, would likely not support or amplify streamwise vortices (the flow is not centrifugally unstable) and that, therefore, large forcing amplitudes would be required to generate streamwise vortices of considerable strength. This was, however, perceived to be of a lesser concern as such structures can be generated by passive means which require no external power. In the experiment steady streamwise vortices could be introduced through, e.g., vortex generators (VGs), isolated roughness elements, steady VGJs, or plasma actuators. In fact, Lake et al. successfully demonstrated separation control for the PackB LPT blade using dimples engraved in the blade surface [18]. Streamwise vortices increase wall-normal mixing and thus reenergize the boundary layer. Vortex generators (VGs) are a passive means for introducing streamwise vortices and have been used successfully in many technical applications such as on airplane wings or in diffusers. Unfortunately, under more favorable operating conditions when flow separation is not a concern, VGs incur losses. A way around this difficulty is to generate streamwise vortices on demand by, e.g., blowing through a spanwise row of discrete holes (VGJs) or by plasma actuators. Experiments showed that VGJs with a blowing ratio (ratio of jet exit velocity to freestream velocity) of 2 that are injected at a skew angle of 90 deg (perpendicular to the flow) and a pitch angle of 30 deg (with respect to the wall) lead to the generation of pronounced streamwise vortices [19].

Despite the large body of publications on flow control for LPT blades, many questions in particular with respect to the VGJ jet actuation parameters remain open. While the effect of pulsing frequency, amplitude, and duty cycle, which can easily be varied in the experiment, were investigated both, experimentally [1,2] and numerically [7,10], the effect of the hole spacing, the jet orientation (normal or angled), and the actuation type (pulsed or harmonic) have not been investigated in great detail. All of these parameters influence the physical mechanisms associated with pulsed VGJ control and hence affect performance. When transitioning pulsed VGJs into real flight hardware investigations that point out dependencies of the AFC effectiveness on such parameters are highly desirable.

Using a high-order-accurate Navier–Stokes code we investigated various separation control techniques for the PackB blade. First, the numerical method and the simulation setup are introduced. Next, results from a grid convergence study for the uncontrolled flow are presented. The flow is then controlled with pulsed VGJs, by harmonic blowing through a slot, by VGJs with wall-normal harmonic blowing, and by steady streamwise vortices. The uncontrolled and controlled flow are analyzed using Fourier transforms in time and in the spanwise direction. For the cases with unsteady flow control the flow is also analyzed using the proper orthogonal decomposition (POD) [20,21] for identifying energetic coherent structures. The paper concludes with a brief discussion of the results.

II.   Computational Approach

A.   Navier–Stokes Code

We employed an in-house developed finite volume code for solving the compressible Navier–Stokes equations on curvilinear grids [22]. The convective terms are computed with a ninth-order-accurate upwind scheme based on a weighted essentially nonoscillatory extrapolation of the characteristic variables and the Roe scheme. A fourth-order-accurate discretization is employed for computing the viscous terms. The governing equations are advanced in time with an implicit second-order-accurate Adams–Moulton method. The resulting system of equations is solved iteratively by a Newton iteration based on a line Gauss–Seidel algorithm and the convergence of the implicit method is monitored by considering the root mean square (rms) of the residuals of all cells for each individual equation. For the time dependent results shown in this paper, the equations were advanced to the next timestep when all rms residuals dropped below 1, which corresponds to a drop of roughly 2 orders of magnitude of the rms residuals. The code was parallelized using the message passing interface library.

B.   Proper Orthogonal Decomposition

POD results in a decomposition of the time dependent flow that, for a given number of modes and for a kernel based on the kinetic energy, captures more of the flows kinetic energy than any other decomposition [20]. We employed the snapshot method [21], which is computationally more efficient than the original method for higher dimensional problems: the POD eigenmodes are computed from

$$\mathbf{q}_i = \sum_n r_i^n \mathbf{v}^n \qquad (1)$$

where the superscript n indicates the timestep ($n = 1 \dots N$), $\mathbf{v}$ is the velocity vector, and r_i are individual elements of $\mathbf{r}_i$, which are eigenvectors of the algebraic eigenvalue problem

$$\mathbf{C}\,\mathbf{r}_i = \lambda_i \mathbf{r}_i \qquad (2)$$

The correlation tensor $\mathbf{C}$ is defined as $C^{nn'} = (\mathbf{v}^n(\mathbf{x}), \mathbf{v}^{n'}(\mathbf{x}))_\Omega / N$. Here, brackets denote an inner product $(\mathbf{a}, \mathbf{b})_\Omega = \int_\Omega \mathbf{a}(\mathbf{x})^T \cdot \mathbf{b}(\mathbf{x})\,d\mathbf{x}$. The eigenfunctions are normalized by their corresponding eigenvalues, $(\mathbf{q}_i, \mathbf{q}_{i'})_\Omega = \delta_{ii'}\lambda_i$, and the time-coefficients are computed as

$$a_i(t) = \frac{1}{\lambda_i}(\mathbf{v}(t), \mathbf{q}_i)_\Omega \qquad (3)$$

POD modes that describe traveling structures appear in pairs. The time-averaged total kinetic energy of the flow is

$$\langle e(t) \rangle = \frac{1}{2}\sum_i \lambda_i \qquad (4)$$

where the kinetic energy of each individual POD mode is $\lambda_i/2$. The original data can be reconstructed/recovered from the eigenmodes and time-coefficients

$$\mathbf{v}(\mathbf{x}, t) = \sum_i a_i(t)\mathbf{q}_i(\mathbf{x}) \qquad (5)$$

The POD modes form an orthogonal basis and are (here) sorted according to their respective energy contents.

C.   Defining Parameters

The blade geometry for our numerical simulations is the Pratt and Whitney PackB LPT blade (Fig. 1) which was also subject of earlier experimental and numerical investigations [1–14]. The ratio of blade spacing, d, and axial chord, C_x, was 0.88. The blade has design inflow and outflow angles of 55 and 30° (both measured from the plane of the cascade). The reference conditions of the case which showed the largest separated flow region in the PackB experiments [1–3] were chosen for the current simulations: All simulations were carried out for a Reynolds number based on axial chord of 25,000 (experiments [1–3]: axial chord $C_x = 7$ inch = 0.1778 m). For our simulations the reference Mach number was set to 0.1 for accelerating the convergence of the implicit part of the flow solver. The same inflow Mach number was also chosen in earlier PackB simulations [4–10]. The inflow temperature was set to 300 K, the ratio of specific heats was $\gamma = 1.4$, and the Prandtl number was 0.72. If not indicated otherwise, length scales were normalized with the axial chord length and velocities were normalized with the inlet velocity.

D.   Computational Grid

In our simulations, both the number of blades and the span were assumed to be infinite (periodic boundary conditions). Following Rizzetta and Visbal [4] who performed a grid size study for the PackB blade, the spanwise extent of the computational domain, ΔZ, was set to $0.2C_x$. We generated grids with 3 different grid resolutions, coarse, medium, and fine. Each of these grids consisted of 5 blocks, where the block structure is shown in Fig. 1. The grids were generated such that continuity of neighboring cells at the boundaries of each block was ensured. Grid points were clustered near the wall, in the separated flow region on the suction side of the blade, and in the wake. The upstream and downstream extent of the computational domain measured from the leading and trailing edge in the streamwise direction was $1.7C_x$ and $1.3C_x$. Table 1 summarizes the block and total grid resolutions of the 3 different grids employed for the present simulations.

Near-wall grid resolutions in wall units for the uncontrolled flow are shown in Fig. 2. The arclength, s, was measured from the leading edge of the blade in clockwise direction. The trailing edge is located at $C_s = 1.46$, the total circumference around the entire blade is 2.74. The grid line spacing, Δn, was normalized with the local v_{wall}/u_τ, e.g.

$$\Delta n^+ = \frac{u_\tau}{v_{\text{wall}}}\Delta n \qquad (6)$$

where v is the molecular kinematic viscosity. The local friction velocity was obtained from the spanwise vorticity, ω_z, at the wall computed from the temporal and spanwise average of the flow data
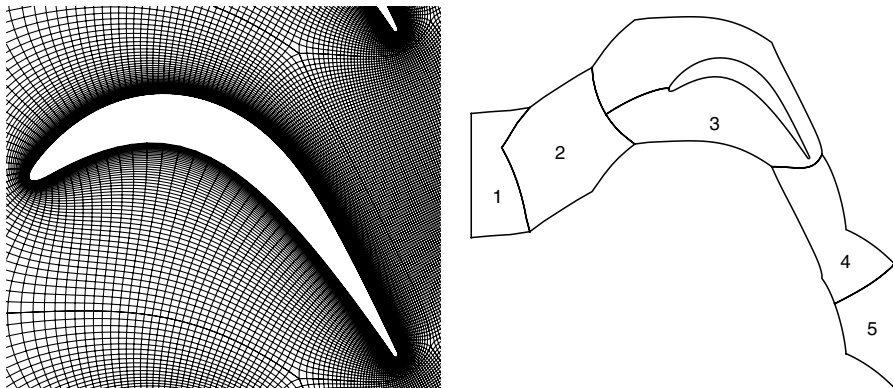

Fig. 1   Coarse computational grid. Detail and block structure.

Table 1   Block grid resolutions

Block	Coarse	Medium	Fine
1	5×15	10×30	20×60
2	10×10	20×20	40×40
3	250×50	500×100	1000×150
4	130×50	260×100	520×200
5	52×55	105×110	210×220
Cells in z	16	32	64
Total	352,560	2,824,000	19,392,000

Table 2   Suction side near-wall grid resolutions

	$s/C_s = 0.11$			$s/C_s = 0.61$			$s/C_s = 0.94$		
	Δs^+	Δn^+	Δz^+	Δs^+	Δn^+	Δz^+	Δs^+	Δn^+	Δz^+
Coarse	54	1	40	6	0.12	10	14	0.27	28
Medium	27	0.5	20	3	0.06	5	7.3	0.13	14
Fine	13	0.58	10	1.5	0.07	2.5	3.7	0.15	7

$$u_\tau = \sqrt{\nu_{\text{wall}} |\omega_z|} \tag{7}$$

Another option would be to employ a reference friction velocity taken at a specific location on the blade. That, however, would introduce some ambiguity. For example, as the point of separation is approached the wall vorticity and for that reason also the friction velocity approach zero. Maximum near-wall grid resolutions in wall units upstream of separation ($s/C_s = 0.11$), in the separated flow region ($s/C_s = 0.61$), and in the reattachment region ($s/C_s = 0.94$) are provided in Table 2. The wall-normal grid resolution in wall units, Δn^+, is close to or smaller than 1 for the coarse grid and half that number for the medium and fine grid. The streamwise and spanwise grid resolutions for the coarse and fine grid are roughly half and twice the respective values for the medium grid. For comparison, the grid resolutions in wall units (normalized by the wall shear taken just upstream of separation) in the streamwise, wall-normal, and spanwise directions for the baseline grid in simulations by Rizzetta and Visbal were 3.1…50.6, 0.3, 6.5, respectively [4]. The formal order of accuracy of the code is one factor that determines the required grid resolution. Rizzetta and Visbal employed a fourth-order-accurate compact scheme coupled with a sixth-order-accurate filter for their simulations.

E.   Boundary Conditions

A characteristics based nonreflecting boundary condition was employed at the inflow and outflow boundaries [23]. The turbine blade wall was considered to be adiabatic. All other boundaries were treated as periodic boundaries. We also deliberately decided to not consider freestream turbulence, unsteady wakes shed by upstream stages, and surface roughness. This constitutes a considerable simplification compared with the environment in real jet engines. However, it allows for an easier identification and extraction of the flow physics associated with separation, transition, and flow control.

F.   Initialization and Time Averaging

The flowfields for the uncontrolled flow were initialized with the inlet conditions and then computed until the time-dependent global behavior of the flow (e.g. lift and drag coefficients) attained a quasi steady behavior (no drift in running time averages, see Table 3). For

Table 3   Startup and time-averaging time intervals

Case	Before time averaging		Time averaging	
Uncontrolled, coarse, and medium	20		20	
Uncontrolled, fine	4		4	
Jets, $B = 1$, $\lambda_z = 0.2$	3		5	
Jets, $B = 2$, $\lambda_z = 0.2$	3		5	
Slot	5		5	
Jets, $B = 0.39$, $\lambda_z = 0.2$	3		5	
Jets, $B = 0.23$, $\lambda_z = 0.0667$	3		5	
Streamwise vortices	$A = 1$	$A = 10$	$A = 1$	$A = 10$
$\lambda_z = 0.05$	1	2	2	2
$\lambda_z = 0.05$, fine grid	-	1	-	1
$\lambda_z = 0.0667$	1	2	2	2
$\lambda_z = 0.1$	1	2	2	2
$\lambda_z = 0.2$	1	1	2	2

the medium resolution uncontrolled flow the time-average was averaged in the spanwise direction and statistical quantities (with respect to this average) were computed over an additional time interval of 20. For all other cases statistical data were not computed. Because of the significant computational expense associated with the fine grid we decided on a rather short time-averaging interval of 4. With a suction side wall tangential velocity of approximately 1.9 and a suction side arclength of 1.46 this dimensionless time of 4 amounts to roughly 5.2 flow over times. All controlled flow simulations were initialized with the uncontrolled flow and advanced in time over a sufficiently long time interval to allow transients to die out before the time-averaging was started.

III.   Results-Uncontrolled Flow

A.   Instantaneous Flow Visualizations and Mean Flow

We employed three different grids (coarse, medium, and fine; Table 1) for the uncontrolled flow simulations. Shown in Fig. 3 are instantaneous visualizations using the vortex identification criterion [24]

$$Q = \frac{1}{2}(W_{ij}W_{ij} - S_{ij}S_{ij}) \tag{8}$$

and the spanwise vorticity

$$\omega_z = \frac{\partial u}{\partial y} - \frac{\partial v}{\partial x} \tag{9}$$

A positive Q criterion indicates areas where rotation dominates strain. Distributions of the wall-pressure and skin friction coefficient

$$c_p = \frac{p - p_{\text{in}}}{\frac{1}{2}\rho_{\text{in}} v_{\text{in}}^2} \tag{10}$$

$$c_f = \frac{\mu \frac{\partial v}{\partial n}}{\frac{1}{2}\rho_{\text{in}} v_{\text{in}}^2} \tag{11}$$

computed from the spanwise and temporal average of the flow are shown in Fig. 4. For comparison, experimental wall-pressure data by Sondergaard et al. (blade #6 measurements from experiments documented in [3]) and Huang et al. [14] as well as data from a direct numerical simulation (DNS) by Rizzetta and Visbal [4] and from a
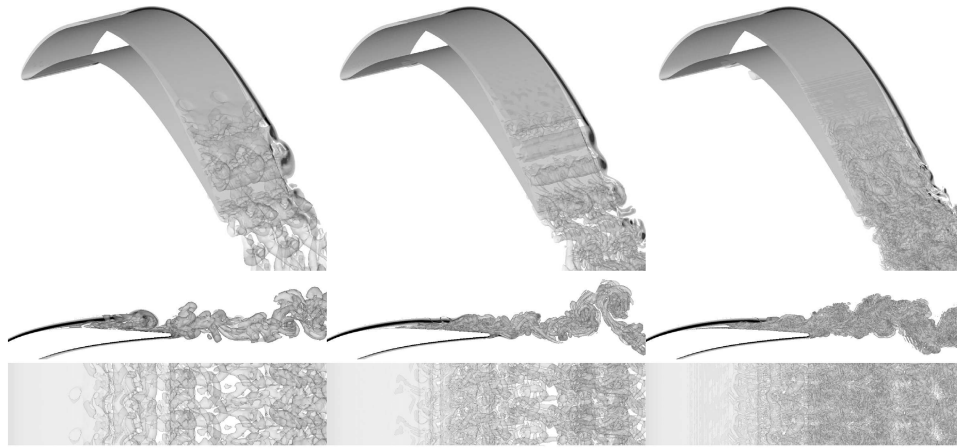
Fig. 2   Streamwise s^+, wall-normal n^+, and spanwise z^+ near-wall grid line spacing in wall units.

Fig. 3   Isosurfaces of vortex identification criterion $Q = 1$ and isocontours of spanwise vorticity ω_z, at $z = 0$. From left to right: coarse, medium, fine grid solution. From top to bottom: perspective view of blade, side view of wake, and top down view of wake. Computational domain was repeated once in spanwise direction.
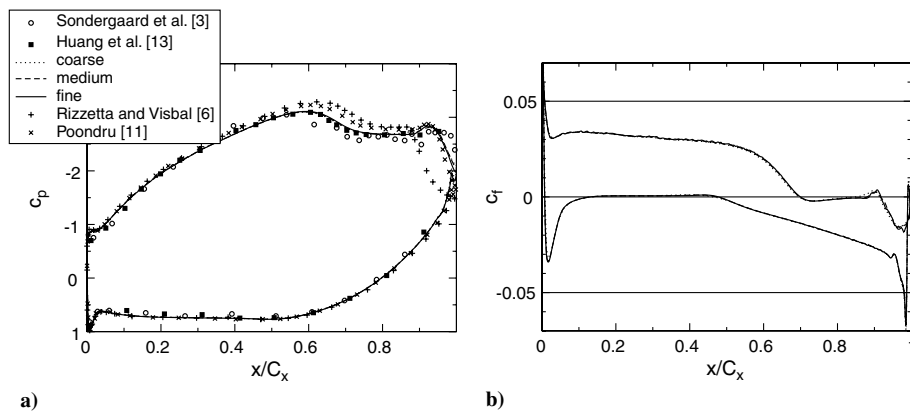

Fig. 4   Graphs of a) wall-pressure and b) skin friction coefficient.

large eddy simulation (LES) with dynamic Smagorinsky model by Poondru [11] were included. Our simulation results are in excellent agreement which each other and with the measurements for the wall-pressure coefficient. In the simulations by Rizzetta and Visbal [4] and Poondru [11] the extent of the separation is underpredicted. Isocontours of the streamfunction distribution (of the temporal and spanwise average of the flow) are shown in Fig. 5 (the stream-function, Ψ, is defined such that $u = \partial\Psi/\partial y$ and $v = -\partial\Psi/\partial x$). Size and shape of the laminar separation bubble nearly coincide for all 3 grid resolutions. The laminar boundary layer on the suction side separates at 70% axial chord (in the mean, Fig. 4b) which is approximately the beginning of the uncovered turning. The separated flow region can be associated with a pressure plateau. The skin friction in the upstream part of the bubble is very low. This stagnant or
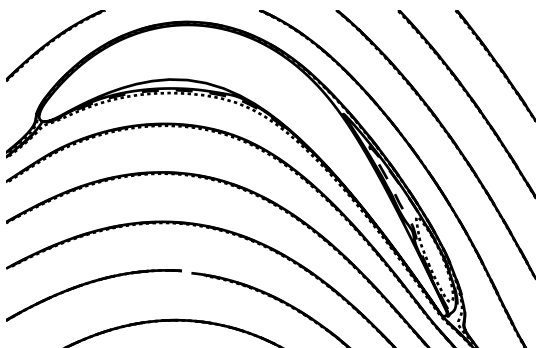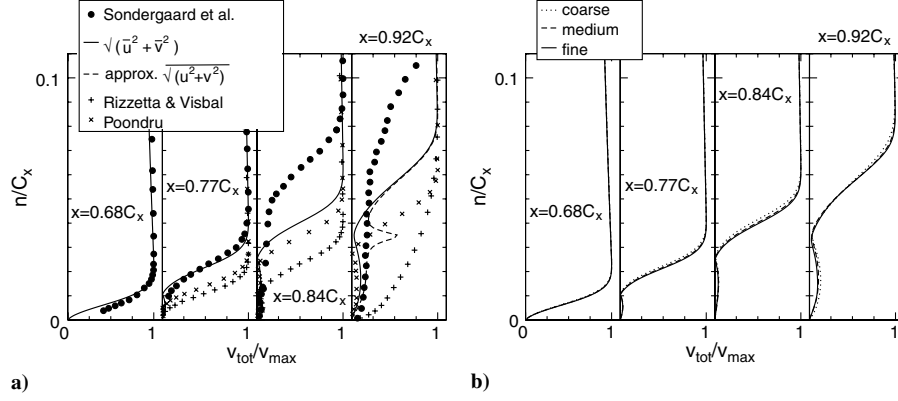
dead air region is situated under the separated laminar boundary layer. Downstream of the maximum bubble height hydrodynamic instabilities of the separated boundary layer and the bubble (inflectional velocity profile, Kelvin–Helmholtz instability) result in a strong disturbance amplification, leading to a roll up of the separated boundary layer and the formation of spanwise vortical structures. These structures increase wall-normal mixing, leading to a sharp increase in negative c_f, the closing of the bubble, and a rapid wall-pressure increase. The secondary separation (in the time mean) near 90% chord can be attributed to the strong 2D spanwise coherent structures. Investigations of a generic separation bubble on a flat plate in a wind tunnel for a chord Reynolds number of 100,000 by Sohn et al. [25] showed a similar behavior of the skin friction distribution. The viscous shear stress in the laminar upstream part of the bubble (dead air region) was found to be very small. Because the distur-bances that seed the spanwise structures were not introduced deliberately into the flow and since the wake shedding was self-sustained one may speculate that the flow was absolutely unstable. On the other hand, one has to remember that a compressible flow solver and highly stretched computational grids were employed. Solving the compressible equations allows for acoustic waves that can travel upstream and disturb the flow. Acoustic noise was found to originate from flow structures that were passing over the trailing edge or through areas of high grid distortion.

A secondary instability mechanism leads to the amplification of three-dimensional (3D) disturbances resulting in the appearance of 3D structures near the trailing edge and in the wake. The 3D structures weaken the coherence of the spanwise structures, resulting in an enlargement of the separation bubble when compared with 2D simulations [10,16]. Instantaneous side and top down views of the wake are shown on the bottom of Fig. 3. The most pronounced

Fig. 5   Isocontours of streamfunction Ψ. Dotted lines: coarse grid; dashed lines: medium grid; and solid lines: fine grid.

Fig. 6 Wall-normal velocity profiles: a) comparison of medium grid results with measurements [3] and other simulations [4,11]; b) comparison of coarse, medium, and fine grid results.

difference between the three results is the increasing amount of random 3D turbulent motion especially near the trailing edge and in the wake as the grid resolution is increased, or in other words, the reduction of the dimensions of the smallest resolved structures.

When resorting to Fig. 3 one may argue that better resolution does not improve the quality of the time-averaged solution (in the separation bubble region) because the turbulent motion is mainly confined to the wake region. A second observation that can be made from Fig. 3 is that the wake turbulence appears to be concentrated in lumps. In analogy to other wake flows, the blade is shedding counter-rotating coherent structures. From side and top down views of the wake, the spanwise coherent structures appear as spanwise concentrations of small-scale turbulent motion.

Wall-normal profiles (normalized by the local velocity maxima) and wake profiles (normalized by the inlet velocity and taken perpendicular to the design exit flow direction at a distance d from the trailing edge) of the velocity magnitude extracted from the temporal and spanwise average of the flow field are shown in Figs. 6 and 7. For comparison measurements by Sondergaard et al. [3] and data obtained from a DNS by Rizzetta and Visbal [4] (profiles at $x/C_x = 0.75, 0.85,$ and 0.95) and a LES with dynamic Smagorinsky model by Poondru [11] (profiles at $x/C_x = 0.75, 0.85,$ and 0.90) were included. Because a single hot wire probe was used in the experiments, no flow direction information was available, and reverse flow could not be resolved. In fact, with the hot wire $\overline{\sqrt{u^2 + v^2}}$ is recorded where the overbar indicates a time-average while the profiles from the simulations show $\sqrt{\overline{u}^2 + \overline{v}^2}$. An approximation[‡] allows for a more direct comparison of the medium grid simulation data for which statistical data was computed with the measurements. Our profiles show good grid convergence and good agreement with the experimental data at $x = 68\%C_x$ and $77\%C_x$. However, at $x = 84\%C_x$ and $92\%C_x$ the profiles indicate a thicker bubble in the experiment. Because the approximation for $\overline{\sqrt{u^2 + v^2}}$ also differs from the experimental data the mismatch cannot be explained by the different time-averaging procedures. In the simulations by Rizzetta and Visbal [4] and Poondru [11] the size of

the separation bubble is underpredicted even more. This observation is consistent with the respective wall-pressure distributions (Fig. 4). At this point, we cannot offer a conclusive explanation for the pronounced mismatch between our calculated and the experimental velocity profiles at $x = 0.84$ and 0.92. Transition and separation are both sensitive to freestream turbulence and geometric imperfections. In the simulations the inflow turbulence is zero and the surface is perfectly smooth. Such ideal conditions cannot be obtained in the experiment. From our simulations we know that an earlier transition will weaken the spanwise structures (rollers) and result in an enlarged separation. This statement is based on a comparison of earlier 2D and 3D simulations where we found the extent of the separated flow region to be smaller in the former [7]. This was argued to be due to the stronger wall-normal momentum exchange facilitated by laminar 2D rollers when compared with spanwise structures superimposed with small-scale 3D motion. One may think of other possible explanations for the mismatch between the numerical and experimental data. Until we have further evidence, all of these arguments will, however, remain speculative. Therefore, at this point we acknowledge the mismatch and postpone any final conclusions until later.

B. Comparison of Flow Dynamics

The flow was also analyzed with respect to the dynamics of the flow structures in the separation bubble. Vortical structures can be detected by considering the wall skin friction coefficient. The skin friction coefficient, $c_f(x, z, t)$, can be Fourier decomposed in the spanwise direction, z

$$c_f = \sum_k c_c^{(k)} \cos\frac{2\pi k z}{\Delta Z} + c_s^{(k)} \sin\frac{2\pi k z}{\Delta Z} \qquad (14)$$

where the respective spanwise wavelengths are $\lambda_z^{(k)} = \Delta Z/k$. Results were computed from data taken over time periods of $\Delta T =$
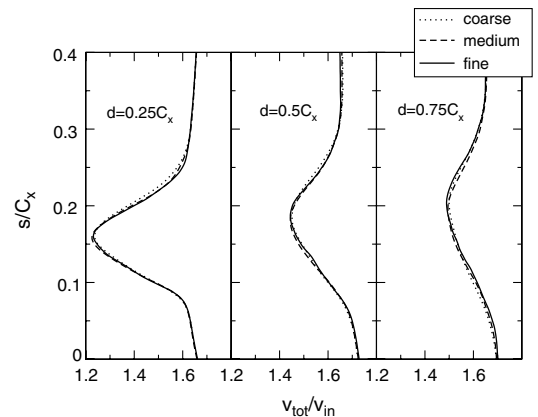
[‡]Taking $f = \sqrt{u^2 + v^2}$ and expanding around the time averages, $\overline{u}$ and $\overline{v}$, using Taylor series

$$f(u, v) = f(\overline{u}, \overline{v}) + u'\frac{\partial f(\overline{u}, \overline{v})}{\partial u} + v'\frac{\partial f(\overline{u}, \overline{v})}{\partial v} + \frac{1}{2}u'^2\frac{\partial^2 f(\overline{u}, \overline{v})}{\partial u^2}$$
$$+ u'v'\frac{\partial^2 f(\overline{u}, \overline{v})}{\partial u \partial v} + \frac{1}{2}v'^2\frac{\partial^2 f(\overline{u}, \overline{v})}{\partial v^2} + \dots \qquad (12)$$

is obtained. This provides the approximation

$$\overline{\sqrt{u^2 + v^2}} \approx \sqrt{\overline{u}^2 + \overline{v}^2} + \left(\frac{1}{2}\overline{v}^2\overline{u'u'} - \overline{u}\,\overline{v}\,\overline{u'v'} + \frac{1}{2}\overline{u}^2\overline{v'v'}\right)(\overline{u}^2 + \overline{v}^2)^{-1.5} \qquad (13)$$

which fails in regions where the velocity magnitude goes to zero.
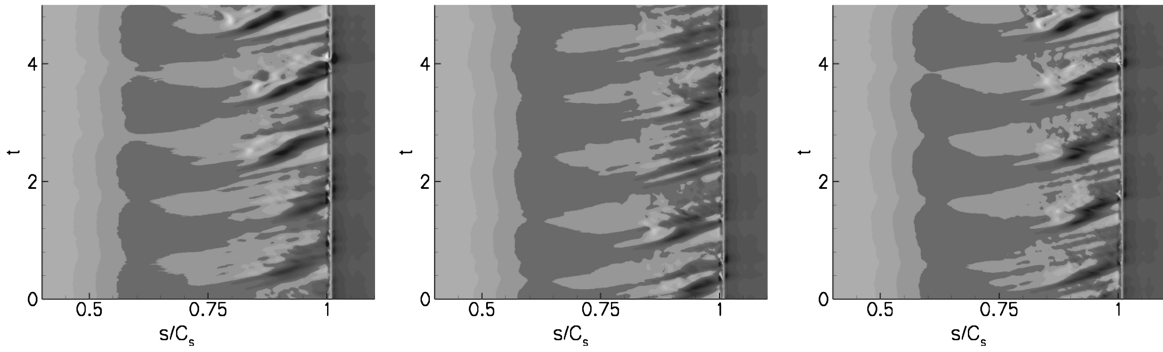

Fig. 7 Wake velocity profiles.

Fig. 8 Space-time diagrams of spanwise average (mode $k = 0$) of skin friction coefficient, c_f. Contour levels: $-0.1 \ldots 0.1$, $\Delta = 0.01$. From left to right: coarse, medium, and fine grid data.

10 (coarse and medium grid) and $\Delta T = 5.5$ (fine grid). In Fig. 8, t versus s diagrams of $\sqrt{c_c^{k=0}(t)^2 + c_s^{k=0}(t)^2}$ are shown. The mode $k = 0$ amplitude distributions illustrate the "footprints" or wall traces of the spanwise coherent structures. The time-derivative of the traces is equivalent to the wave speed of the structures and approximately the same for all cases. The natural vortex shedding frequency of the separation bubble, which can be determined by measuring the time-difference between the most pronounced wall traces, is about 1. Vortex merging (subharmonic resonance) of the spanwise structures, where the wall traces of two spanwise coherent structures merge into one, cannot be observed. The appearance of the $k = 1$ mode (or first 3D mode, Fig. 9) seems linked to the presence of the 2D mode ($k = 0$). It can be speculated that the growth of the 3D mode is caused by a secondary instability of the time-dependent 2D flow.

The skin friction coefficient, $c_f(x, z, t)$, can additionally be Fourier decomposed in time, t

$$
c_f = \sum_n \sum_k \left(c_{cc}^{(n,k)} \cos \frac{2\pi nt}{\Delta T} + c_{cs}^{(n,k)} \sin \frac{2\pi nt}{\Delta T} \right) \cos \frac{2\pi kz}{\Delta Z}
$$
$$
+ \left(c_{sc}^{(n,k)} \cos \frac{2\pi nt}{\Delta T} + c_{ss}^{(n,k)} \sin \frac{2\pi nt}{\Delta T} \right) \sin \frac{2\pi kz}{\Delta Z} \tag{15}
$$

where the respective oscillation frequencies are $f^{(n)} = n/\Delta T$. In Fig. 10a, frequency spectra of mode $k = 0$ of the wall-pressure coefficient, c_p, are shown for three downstream locations. Wall data was output every eighth timestep for the coarse and medium grid simulation (simulation timestep $\Delta t = 0.0005$) and every fifth timestep for the fine grid simulation ($\Delta t = 0.002$), which relates to frequencies of $f = 1/0.004 = 250$ and $f = 1/0.01 = 100$, which are lower than the Nyquist frequency, $f = 2/\Delta t$. The spectra in Fig. 10a were plotted with a linear scale for the frequency to allow for an easier comparison of the low-frequency part of the spectra. The fundamental ($f \approx 1$) grows in amplitude by roughly 1 order of
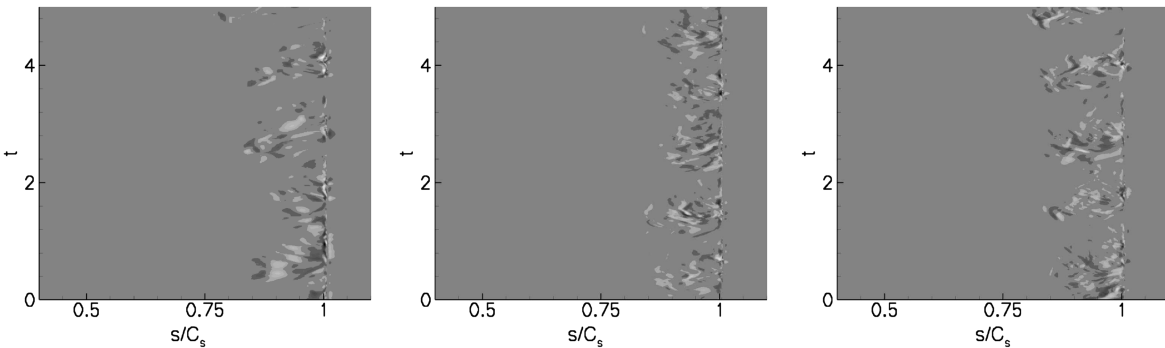

Fig. 9 Space-time diagrams of first 3D mode (mode $k = 1$) of skin friction coefficient, c_f. Contour levels: $-0.1 \ldots 0.1$. From left to right: coarse, medium, and fine grid data.
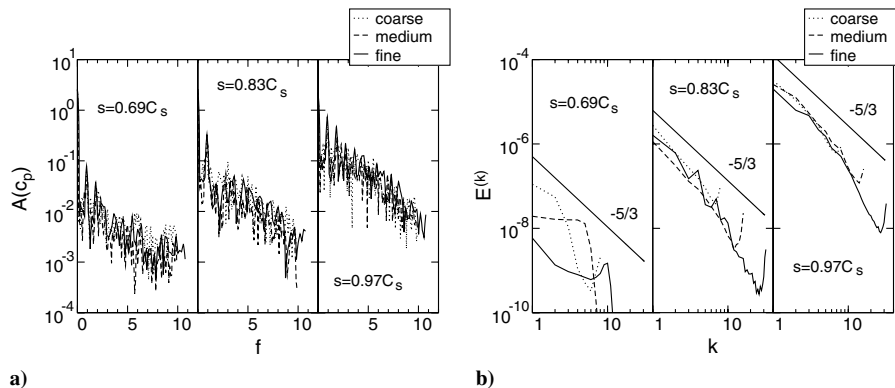

Fig. 10 Graphs of a) frequency spectra of mode $k = 0$ of wall-pressure coefficient c_p, and b) estimates of energy spectral density and $-5/3$ slope of inertial subrange.

magnitude between $s/C_s = 0.69$ and 0.97. For $s/C_s = 0.97$, the spectrum begins to fill up as the flow transitions to turbulence and higher harmonics of appreciable amplitude appear. The low-frequency part of the spectra which contains the bulk of the kinetic energy is approximately identical in all three cases, again indicating grid convergence of the solution (with respect to the flow dynamics of the separation bubble).

Assuming inviscid flow, a local inviscid wall velocity can be computed from the wall-pressure coefficient

$$v = v_{\text{in}} \sqrt{1 - c_p} \qquad (16)$$

An estimate of the energy spectral density

$$E^{(k)}(x) = \frac{\overline{c_c^{(k)}(x,t)^2 + c_s^{(k)}(x,t)^2}}{4 \frac{2\pi}{\Delta Z}} \qquad (17)$$

can be obtained from the spanwise Fourier coefficients of the inviscid wall velocity,

$$c_c^{(k)}(x,t) = \frac{2}{K} \sum_{l=1}^{K} v(x, z_l, t) \cos \frac{l-1}{K} 2\pi k$$

$$c_s^{(k)}(x,t) = \frac{2}{K} \sum_{l=1}^{K} v(x, z_l, t) \sin \frac{l-1}{K} 2\pi k \qquad (18)$$

where K is the total number of cells in z.

Distributions of the energy spectral density estimate for the uncontrolled flow are shown in Fig. 10b. Also included is the $-5/3$ slope of the inertial subrange. At $s = 0.69 C_s$ the flow is mainly 2D and the energy content of the higher spanwise modes is practically zero. For $s = 0.83 C_s$ and $s = 0.97 C_x$ the higher modes fill up indicating the onset of transition. Also, the energy spectra coincide, thus indicating grid independence of the solution. The energy spectral density estimate does not drop down to machine accuracy for $k \gg 0$ but instead an energy accumulation can be observed at the high wavenumber end. This indicates that the simulations are not fully resolved for all three grid resolutions and that the dissipation range is not captured. Because the low wavenumber part of the energy spectra for all 3 grid resolutions and the mean flow results nevertheless coincide we suspect that the error introduced by the lack of resolution is sufficiently small to not affect the overall result. We consequently refer to the present simulations as implicit large eddy simulations or underresolved direct numerical simulations.

For the medium resolution grid, we also computed Favre-averaged turbulence quantities, the Reynolds stresses, $\overline{v_i' v_j'}$, the turbulence kinetic energy, $k = 1/2 \overline{v_i' v_i'}$, and the dissipation, $\varepsilon = 2\nu \overline{s_{ij}' s_{ij}'}$. Spanwise averages of the turbulence quantities are shown in Fig. 11. The Reynolds stresses, the turbulence kinetic energy, and the turbulence dissipation obtain considerable magnitudes in the reattachment region near the trailing edge of the blade. The normal stresses are not of the same magnitude indicating anisotropy of the turbulence and hinting at the presence of 2D coherent structures. This is supported by the observation that the $\overline{u'v'}$ component is larger than the $\overline{v'w'}$ and $\overline{w'u'}$ components. A comparison of wall-normal profiles of $\overline{u'u'}$ and $\overline{u'v'}$ is provided in Fig. 12. The Reynolds stress magnitudes in the LES with dynamic Smagorinsky model by Poondru [11] are larger than in the present simulation. This may explain the earlier closing of the separation bubble in the LES when compared with the present results.

Finally, the physical grid resolution can be estimated by considering the local ratio of grid resolution, $\max(\Delta x, \Delta y, \Delta z)$, and Kolmogorov length scale

$$L_k = \left(\frac{\nu^3}{\varepsilon} \right)^{\frac{1}{4}} \qquad (19)$$

which is the length scale of the smallest dissipating eddies in the flow. Results for the medium resolution grid are shown in Fig. 13. The grid spacing near the trailing edge is approximately 10 times the Kolmogorov length scale. For a true DNS, this resolution is
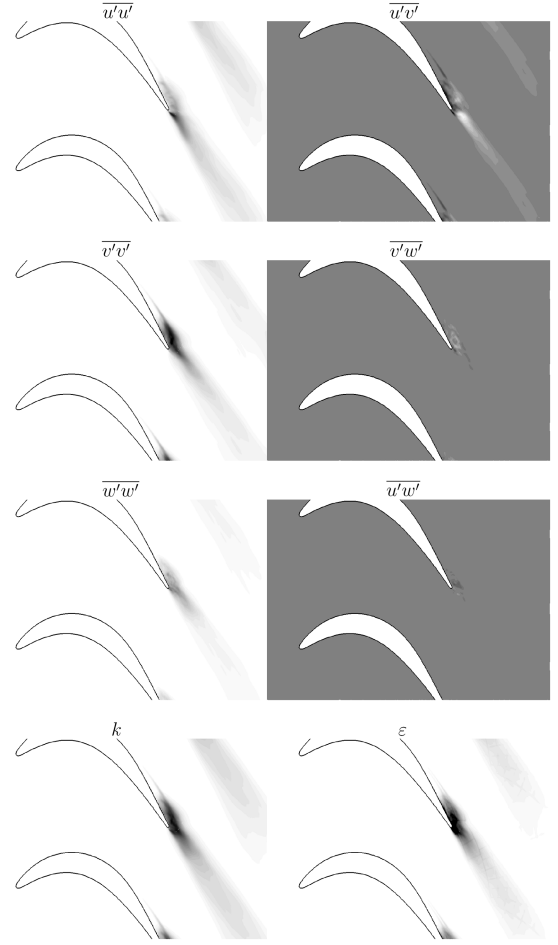
Fig. 11 Spanwise averages of Favre-averaged Reynolds stresses $\overline{u_i' u_j'}$, turbulence kinetic energy k, and dissipation ε for medium resolution grid. Contour levels: $0 \ldots 0.4$, $\Delta = 0.01$ for $\overline{u'u'}$, $\overline{v'v'}$, $\overline{w'w'}$, k, and ε; $-0.1 \ldots 0.1$, $\Delta = 0.01$ for $\overline{u'v'}$, $\overline{v'w'}$, and $\overline{w'u'}$.

insufficient and may result in an underprediction of turbulent mixing in the simulations and an overprediction of the strength of the spanwise structures and a reduction of the bubble size. Because we, however, found our coarse, medium, and fine grid results to be sufficiently grid resolved with respect to both the time-averages and the flow dynamics we speculate that the numerical diffusion provided by the higher-order-accurate upwind schemes employed in the present simulations provided for adequate dissipation at the smallest resolved scales. Margolin and Rider [26] showed that certain upwind schemes exhibit similar diffusion characteristics at the smallest
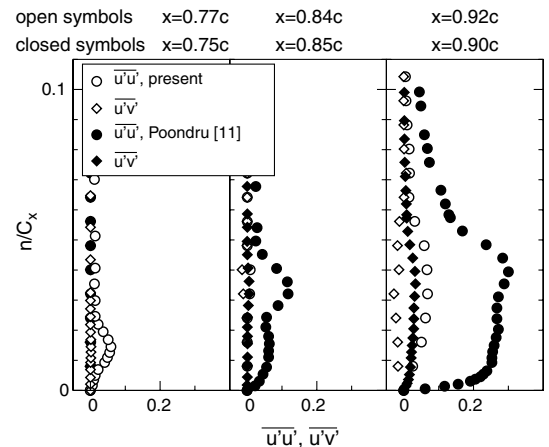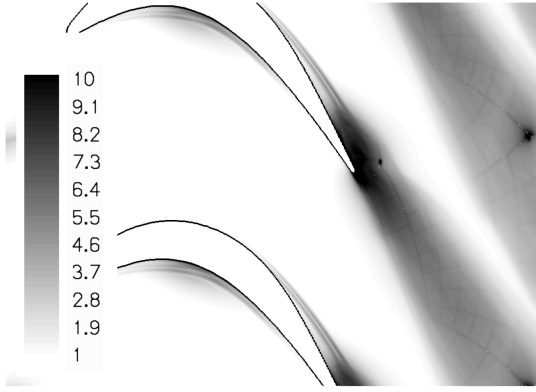

Fig. 12 Wall-normal Reynolds stress profiles.

Fig. 13 Physical grid resolution $\max(\Delta x, \Delta y, \Delta z)/L_k$ for medium resolution grid.

resolved scales as standard subgrid scale turbulence models used in LES.

IV. Results-Controlled Flow

We investigated separation control by pulsed VGJs, by harmonic blowing through a slot, by harmonic blowing through VGJ holes, and by steady streamwise vortices. For the flow control investigations we employed the medium resolution grid assuming that the preceding grid resolution study for the uncontrolled flow was proof enough that the medium resolution grid would also offer sufficient resolution for the cases with flow control.

A. Flow Control Strategies

For pulsed VGJ control we employed a reduced duty cycle forcing where the jet exit velocity is

$$v_f(t) = \begin{cases} Bv_{in} & \text{if } 0 \le t \le \tau T \\ 0 & \text{if } \tau T < t < T \end{cases} \qquad v_f(t + T) = v_f(t) \qquad (20)$$

The duty cycle τ, which is defined as the ratio of *control on* duration to period, T, was 10% (experiments: Bons et al. [1]: $\tau = 50\%$, Huang et al. [14]: $\tau = 10\%$). The forcing period was $T = 0.2$ and the forcing frequency was $f = 1/T = 5$. The forcing period in the simulations was based on earlier 2D simulations where we determined the most effective forcing frequency for controlling the separation bubble [7]. In experiments where separation at $Re = 50,000$ was controlled by pulsed plasma actuators, Huang et al. found pulsed actuation with $f \approx 4.8$ (or ≈ 1 based on the length of the separation zone and the local freestream velocity) to be most effective [14]. The forcing frequency in the experiments by Bons et al. [1,2] was $f = 10$ Hz which corresponds to a nondimensional forcing frequency of 0.843[§] and a period of 1.19. The blowing ratio which is defined as the maximum jet exit velocity divided by the inlet velocity, $B = v_f/v_{in}$, was 1 and 2 (experiments [1]: $B = 0.2$). The holes were placed at $x \approx 0.630 C_x$ (same as in Bons et al. [1,2] and Sondergaard et al. [3]), had approximate hole dimensions, $\Delta s \times \Delta z$, of 0.0330×0.0438, and were resolved with 7×7 cells (experiments: hole diameter 0.001 m/0.1778 m = 0.00562). The hole spacing was identical to the spanwise extent of the domain, $\lambda_z = \Delta Z = 0.2 C_x$, meaning that only one VGJ was computed. The hole spacing in the experiments [1–3] was $0.0562 C_x$ which makes the disturbance input more continuous in the spanwise direction (the control had a stronger 2D contribution). The jets where issued into the boundary layer at a 30° pitch angle and a 90° skew angle (same as in experiments).

For the case with harmonic blowing through a slot, a slot of width $b = \Delta s = 0.0144$ which was resolved with 3 cells was positioned at

$x \approx 0.622 C_x$. The wall-normal velocity component over the slot surface was

$$v_f(t) = \frac{1}{2}\left(1 + \cos 2\pi \frac{t}{T}\right)Bv_{in} \qquad (21)$$

The forcing period was 0.2 and the blowing ratio was 0.1. In the experiment a comparable spanwise constant disturbance input could be realized with a plasma actuator.

The momentum coefficient

$$c_\mu = \frac{\iint(\frac{1}{T}\int \rho_f v_f^2 \, dt) \, dx \, dz}{\frac{1}{2}\rho_{in} v_{in}^2 C_x \Delta Z} \qquad (22)$$

is integrated over the forcing slot/ jet exit hole and over one forcing period, T. For the cases considered here the density variation can be neglected, $\rho_f = \rho_{in}$. The momentum coefficient is computed relative to the zero forcing signal and not, as is the case for the oscillatory momentum coefficient, $\langle c_\mu \rangle$, relative to the time-averaged forcing signal. For reduced duty cycle blowing through circular holes with radius, R, and spanwise hole spacing, ΔZ, and assuming a parabolic velocity distribution over the hole (as chosen here)

$$v_f(r, t) = \begin{cases} Bv_{in}\left(1 - \frac{r^2}{R^2}\right) & 0 < t < \tau T \\ 0 & \text{otherwise} \end{cases} \qquad (23)$$

the momentum coefficient becomes

$$c_\mu = \frac{2}{3}\frac{\pi R^2}{C_x \Delta Z}\tau B^2 \qquad (24)$$

Here, the cross-sectional area of the holes was taken as $\pi ab \sin 30° = \pi \times 0.0330/2 \times 0.0438/2 \times \sin 30° = 5.68 \times 10^{-4}$ (experiments [1–3]: 2.48×10^{-5}). For harmonic blowing through a slot the momentum coefficient becomes

$$c_\mu = \frac{3}{4}\frac{b}{C_x}B^2 \qquad (25)$$

We also carried out simulations where we investigated harmonic wall-normal blowing through VGJ holes. The blowing ratio was such that the momentum coefficient

$$c_\mu = \frac{1}{4}\frac{\pi R^2}{C_x \Delta Z}B^2 \qquad (26)$$

(where the hole area, πR^2, is taken as $\pi ab = 1.13 \times 10^{-3}$ and not as $\pi ab \sin 30°$ because the jets are issued in wall-normal direction) was equal to 2 times the momentum coefficient for the slot forcing, resulting in $B = 0.390$ (for one hole per ΔZ, $\lambda_z/C_x = 0.2$) and $B = 0.225$ (for three holes per ΔZ, $\lambda_z/C_x = 0.2/3 = 0.0667$).

Finally, we generated steady streamwise vortices by introducing a volume force for $r_0 < r < r_0 + \Delta r$

$$f_r = A^* \sin\left(\pi \frac{r - r_0}{\Delta r}\right)\cos\left(2\pi k \frac{z}{\Delta Z}\right) \qquad (27)$$

$$f_z = -A^* \sin\left(2\pi \frac{r - r_0}{\Delta r}\right)\sin\left(2\pi k \frac{z}{\Delta Z}\right) \qquad (28)$$

in a circular segment between the angular positions $\vartheta_1 = 53.1°$ and $\vartheta_2 = 39.5°$ as shown in Fig. 14. Thereby $2k$ streamwise vortices with a spanwise wavelength of $\lambda_z = \Delta Z/k$ were generated. Plasma actuators also exert a volume force through the acceleration of charged particles in an electric field. The associated volume force distribution [6] is, however, very different from the volume force distribution proposed here. The present model is somewhat hypothetical and resulted from the need to efficiently introduce streamwise vortices in the numerical simulation. The radius r was measured from the origin ($x_0 = 0.2834$, $y_0 = 0.1896$) and the radius $r_0 = 0.5484$ was chosen such that the resulting circle was closely aligned with the suction side wall of the turbine blade between ϑ_1 and

---

[§]With a Reynolds number based on inlet velocity and chord length of $Re = 25,000$, a kinematic viscosity of $\nu = 1.5 \times 10^{-5}$ m²/s, and a chord length of $C_x = 0.1778$ m the inlet velocity becomes $v_{in} = \nu Re/C_x = 2.11$ m/s. The nondimensional frequency is $fC_x/v_{in} = 10 \times 0.1778/2.11 = 0.843$.
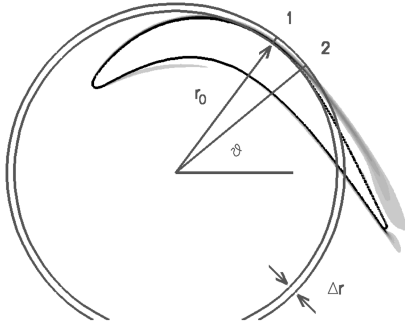
Fig. 14 Isocontours of spanwise vorticity ω_z, computed from temporal and spanwise average of uncontrolled flow. Also indicated is area where streamwise vortices were forced.

ϑ_2. For our simulations, we chose $\Delta r = 0.025$ which is roughly 2 times the local boundary layer thickness. The volume forces were added to the right-hand-sides of the momentum equations, e.g. $\partial \rho w / \partial t + \ldots = f_z$. A momentum coefficient can be defined

$$c_\mu = \frac{\iiint f \, dx \, dy \, dz}{\frac{1}{2} \rho_{\mathrm{in}} v_{\mathrm{in}}^2 C_x \Delta Z} \qquad (29)$$

where $f = \sqrt{f_r^2 + f_z^2}$ and $\Delta r \times \Delta Z / (2k)$ is the wall-normal and spanwise extent of one vortex. The momentum coefficient then becomes

$$c_\mu = 2(\vartheta_1 - \vartheta_2) \frac{2kA}{C_x^2 \Delta Z} \int_0^{\Delta Z/(2k)} \int_{r_0}^{r_0 + \Delta r} \frac{f}{A^*} r \, dr \, dz \qquad (30)$$

where $A = C_x / (\rho_{\mathrm{in}} v_{\mathrm{in}}^2) A^*$ is the nondimensional volume forcing amplitude (or acceleration). This equation can be integrated numerically. Using volume forces (Fig. 14) we introduced streamwise vortices with spanwise wavelengths of $\lambda_z = 0.05, 0.0667, 0.1,$ and 0.2 and nondimensional volume forcing amplitudes of $A = 1$ and 10. As mentioned earlier, since the suction side boundary layer of the turbine blade is convex, streamwise vortices are not amplified and relatively large momentum coefficients were required for generating streamwise vortices. On the contrary, spanwise vortices (which can be generated by harmonic blowing and suction through a slot or by plasma actuators), are amplified by the shear layer instability and, therefore, require comparatively low momentum coefficients. With the current grid resolution of 32 cells in z the resolution limit of 8 cells per wavelength is reached for $\lambda_z = 0.05$. At this resolution, reasonably accurate results can still be expected with the ninth-order-accurate scheme that was employed for the current investigations. Table 4 provides a summary of the momentum coefficients.

B. Unsteady Flow Control—VGJ and Slot Forcing

1. Instantaneous Flow Visualizations

Instantaneous flow visualizations for the cases with unsteady flow control are provided in Fig. 15. All five flow control techniques appear to prevent or at least reduce flow separation. Control with pulsed VGJs (Figs. 15a and 15b) seems to result in earlier transition

Table 4 Momentum coefficients

Case	B	λ_z	c_μ
Pulsed VGJs,	1	0.2	1.9×10^{-4}
30° pitch and 90° skew angle	2	0.2	7.6×10^{-4}
Slot, harmonic blowing	0.1	-	1.1×10^{-4}
Harmonic VGJs,	0.39	0.2	2.2×10^{-4}
Wall-normal jets	0.23	0.0667	2.2×10^{-4}
Streamwise vortices	$A = 1$	0.05, 0.0667, 0.1, 0.2	7.1×10^{-3}
	$A = 10$	0.05, 0.0667, 0.1, 0.2	7.1×10^{-2}

compared with the uncontrolled flow (Fig. 3). With $B = 1$ spanwise coherent structures appear. For $B = 2$ such structures are not immediately evident. Control with harmonic blowing through a slot (Fig. 15c) results in the formation of pronounced spanwise structures (or rollers) and a transition delay compared with the uncontrolled flow. Small-scale 3D motion appears considerably farther downstream in the wake. With harmonic VGJ actuation and $B = 0.390$ (1 hole/ΔZ, $\lambda_z = 0.2$, Fig. 15d) the resulting instantaneous flow field looks similar to the flow field obtained with pulsed VGJs and $B = 1$. When the hole spacing is decreased (harmonic VGJ actuation with $B = 0.225$, 3 holes/ΔZ, $\lambda_z = 0.0667$, Fig. 15e) the spanwise rollers become more coherent and the instantaneous flow visualization looks more similar to the visualization obtained for the slot forcing.

2. Time-Averaged Flow

A more quantitative comparison becomes possible when considering the wall-pressure coefficient c_p (Figs. 16a and 17), the skin friction coefficient, c_f, (Fig. 17), and isocontours of the streamfunction (Fig. 16b). Compared with the uncontrolled flow, flow control results in a significant reduction of the mean separation (Figs. 16a and 17) and a larger suction between 60% and 80% chord combined with a stronger pressure recovery near the trailing edge downstream of 80% chord. The most effective (and efficient considering the momentum coefficient, Table 4) separation control is accomplished for harmonic blowing through a slot. Control with pulsed VGJs and $B = 2$ results in a slightly shorter bubble than forcing with $B = 1$. Harmonic wall-normal VGJ actuation with $B = 0.39$ ($\lambda_z = 0.2$) is equally effective as pulsed VGJ actuation with $B = 2$ but more efficient as the respective momentum coefficient is lower. Postl [10] also found wall-normal injection to be more effective. This was attributed to the larger 2D disturbance input resulting in stronger 2D spanwise coherent structures which were found to be mainly responsible for a successful separation control with pulsed VGJs. In fact when the spanwise hole spacing is reduced to $\lambda_z = 0.0667$ without changing the momentum coefficient the control becomes even more effective (Fig. 17) and the c_p-curve of the slot forcing is approached.

Wall-normal velocity profiles on the blade (normalized by the respective velocity maxima) and wake profiles (averaged in t and z) are shown in Fig. 18. The velocity profiles indicate a thick bubble and a wide wake for the uncontrolled flow. With flow control, the flow is barely separated at 77% chord and separated with weak reverse flow at 84% chord. Fully attached flow is obtained at $x = 0.92C_x$. At this station, fuller velocity profiles are obtained for VGJs with $B = 2$ and reduced duty cycle actuation and with $B = 0.309$ and harmonic actuation (1 hole/ΔZ, $\lambda_z = 0.2$), indicating that the flow is more turbulent. Flow control also results in a reduction of the wake width (Fig. 18b) and, therefore, the wake momentum deficit. The wake velocity profiles for the slot actuation are noticeably different from the wake velocity profiles for the other controlled cases (Fig. 18b). We speculate this to be a consequence of the delayed transition.

3. Analysis of Flow Dynamics

Space-time diagrams of the spanwise average of the skin friction coefficient are shown in Fig. 19. Compared with the uncontrolled flow the wall traces in the space-time diagrams are very regular especially for the slot forcing and VGJs with wall-normal harmonic blowing and $\lambda_z = 0.0667$. A more quantitative comparison becomes possible when considering frequency spectra of the spanwise average (spanwise Fourier mode $k = 0$) of the wall-pressure coefficient at constant streamwise locations. First, the results for pulsed VGJ actuation and harmonic slot forcing are discussed. The spectra in Fig. 20a show pronounced peaks near the forcing frequency and its higher harmonic. At all 3 streamwise stations the highest peak amplitudes are obtained for the slot forcing. At $s = 0.83C_s$ and $s = 0.97C_s$ the peak amplitudes for $B = 1$ are higher than for $B = 2$. In general, with control the disturbance amplitudes for frequencies other than the fundamental and its harmonics are reduced compared with the uncontrolled flow. Similar spectra as for
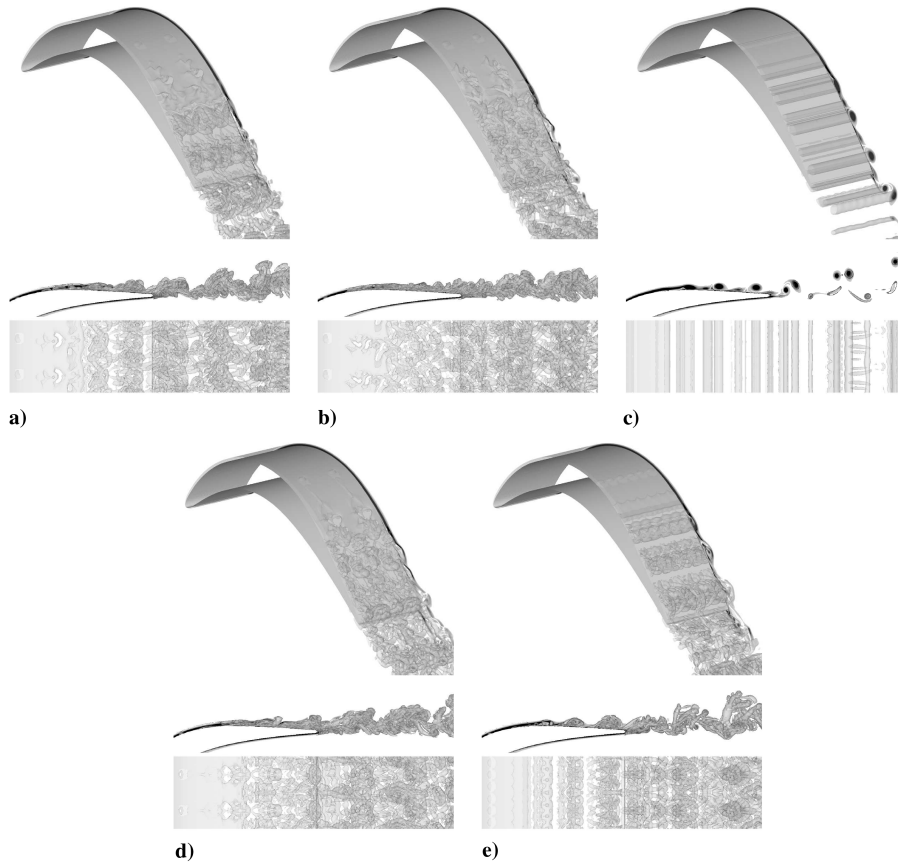
Fig. 15 Isosurfaces of vortex identification criterion $Q = 1$, and isocontours of spanwise vorticity ω_z. Pulsed VGJs with a) $B = 1$, b) $B = 2$, and c) harmonic blowing through slot with $B = 0.1$. Jets with wall-normal harmonic blowing and d) $B = 0.390$, $\lambda_z = 0.2$, and e) $B = 0.225$, $\lambda_z = 0.0667$. From top to bottom: perspective view of blade, side view of wake, and top down view of wake. Computational domain was repeated once in spanwise direction.
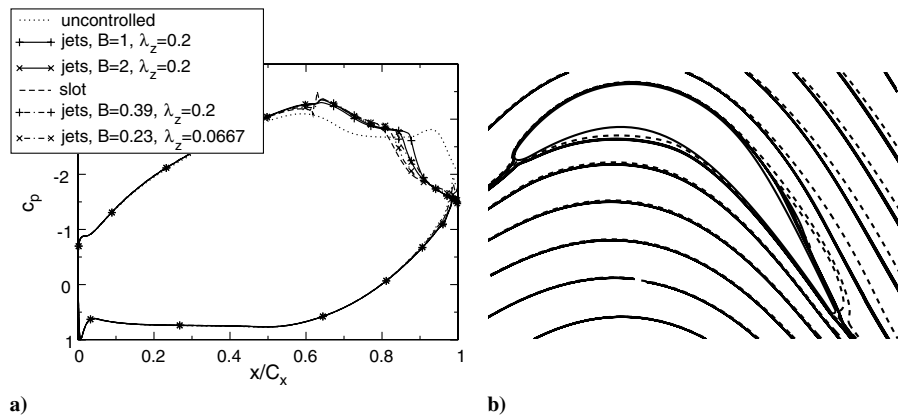

Fig. 16 a) Wall-pressure coefficient and b) isocontours of streamfunction (dashed lines: uncontrolled flow; solid lines: controlled flow).

the slot forcing were seen in the experiments with plasma actuator flow control by Huang et al. [14]. With plasma actuator (which introduces a disturbance that is fairly uniform in the spanwise direction) the general level of the background fluctuations was lowered slightly and very pronounced peaks at the fundamental frequency and its higher harmonics appeared in the spectra.

Further insight is obtained when considering estimates of the energy spectral density computed from the wall-pressure coefficient, Fig. 20b. At $s = 0.69 C_s$ significant 3D mode ($k > 0$) amplitudes are obtained only with pulsed VGJs where the energy contents of the 3D modes is higher for $B = 2$. Both, the uncontrolled flow and the flow with slot actuator are essentially 2D. At $s = 0.83 C_s$ and $s = 0.97 C_s$ the flow remains 2D with slot actuator and the 3D mode amplitudes are noticeably lower than for the uncontrolled flow. With pulsed VGJs at $s = 0.83 C_s$ more energy is contained in the 3D modes than
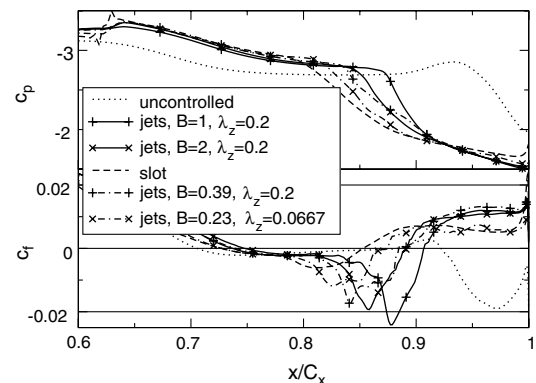

Fig. 17 Wall-pressure coefficient c_p and skin friction coefficient c_f.
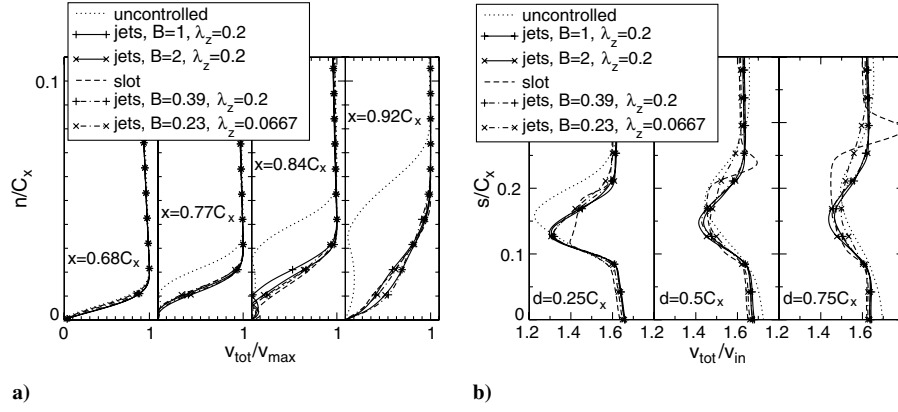
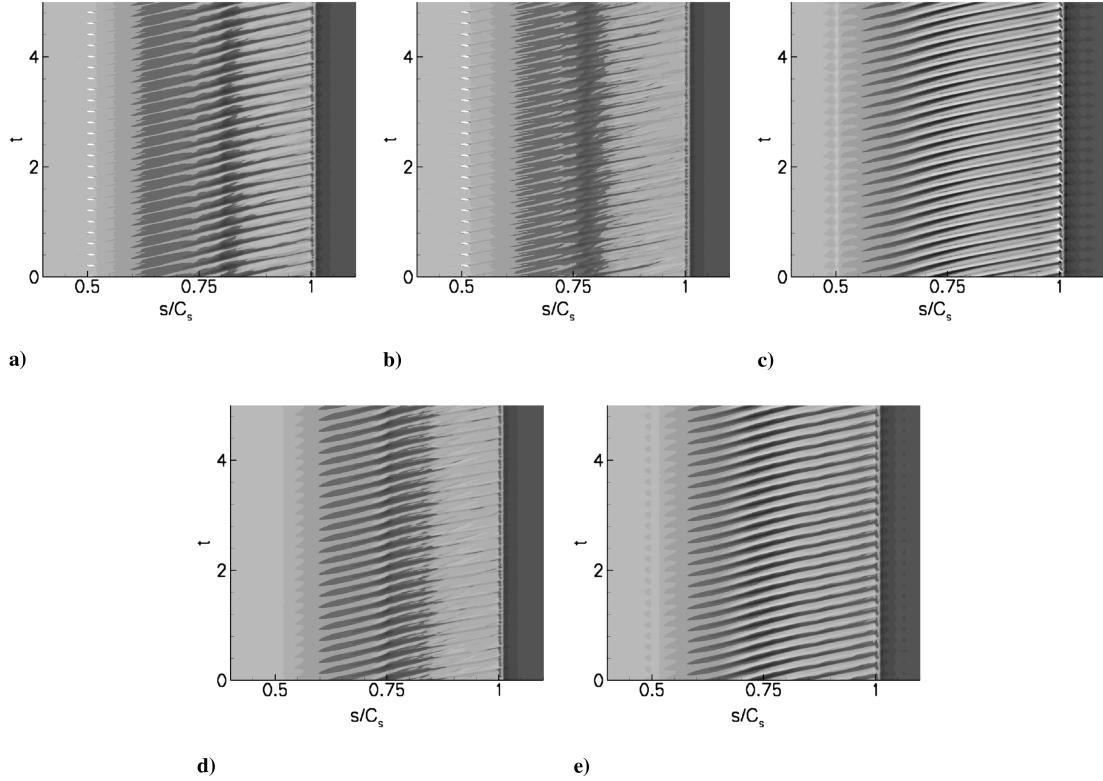Fig. 18   Graphs of a) wall-normal profiles, and b) wake velocity profiles.

Fig. 19   Top: Space-time diagrams of spanwise average of skin friction coefficient c_f. Contour levels: $-0.1 \ldots 0.1$, $\Delta = 0.01$. Pulsed VGJs with a) $B = 1$, b) $B = 2$, and c) harmonic blowing through slot with $B = 0.1$. Jets with wall-normal harmonic blowing and d) $B = 0.390$, $\lambda_z = 0.2$, and e) $B = 0.225$, $\lambda_z = 0.0667$.
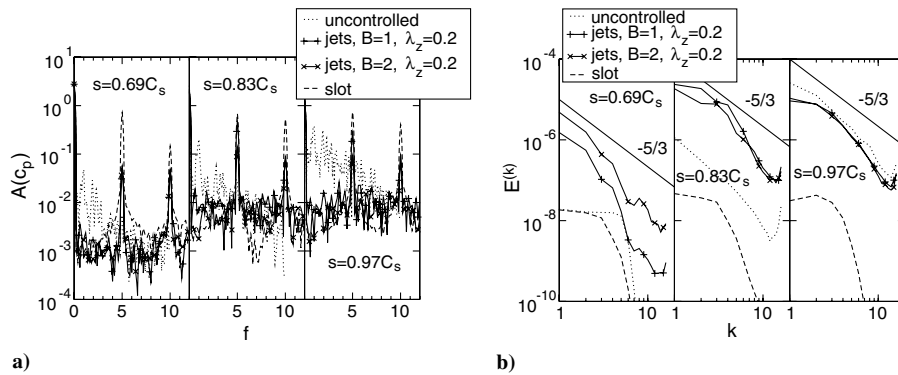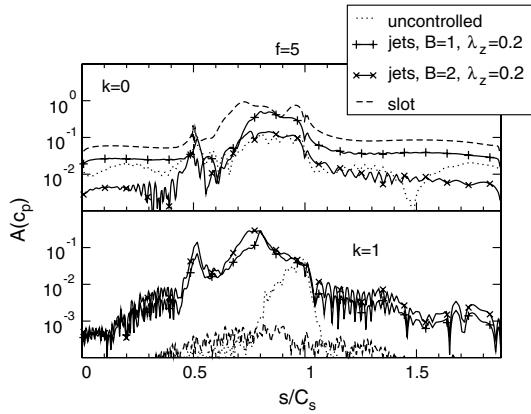

Fig. 20   Graphs of a) frequency spectra of wall-pressure coefficient c_p, and b) estimates of energy spectral density and $-5/3$ slope of inertial subrange.

Fig. 21 Amplitude of $f = 5$ **disturbance component of spanwise modes** $k = 0$ **and 1 of wall-pressure coefficient.**

for the uncontrolled flow indicating earlier transition. At $s = 0.97C_s$ the spectra for the cases with pulsed VGJ control approximately coincide with the spectrum for the uncontrolled flow.

Finally, amplitude distributions of the $f = 5$ and $k = 0$ and 1 disturbances of the wall-pressure coefficient are shown in Fig. 21. For control with harmonic blowing through a slot the $k = 0$ mode experiences linear instability amplification beginning roughly at $s = 0.6C_s$. Around $s \approx 0.7C_s$ saturation is reached. The linear (exponential) amplification in combination with the two-dimensionality of the flow (the 3D modes remain essentially zero) explain the superior effectiveness of this flow control compared with the control by pulsed VGJs. With pulsed VGJs and $B = 1$ linear growth of the 2D mode is also observed, however, starting from a lower amplitude level and reaching saturation farther downstream compared with the case with slot forcing. After saturation is reached, the energy contents of the 2D mode ($k = 0$) is lower for $B = 2$ when compared with $B = 1$ which coincides with the weaker coherence of the spanwise structures in the flow visualizations, Fig. 15. As the momentum coefficient was smaller for the slot actuator than for the pulsed VGJs it can be concluded that the harmonic slot forcing is a more effective method for introducing 2D disturbances than the pulsed VGJs where the 2D disturbance component is introduced by the in-phase actuation of the VGJs.

The reduced duty cycle function [Eq. (20)] can be Fourier transformed in time

$$v_f(t) = \left\{ \frac{a_0}{2} + \sum_n a_n \cos\left[\frac{2\pi}{T} n(t - 0.5\tau T) \right] \right\} B v_{in} \qquad (31)$$

with mode amplitudes $a_0 = 2\tau$ and $a_n = \frac{2}{\pi n} \sin \pi n \tau$. Examples are shown in Fig. 22. A large number of Fourier modes is required for an

accurate representation of the duty cycle function. Conversely, the reduced duty cycle actuation introduces a large number of disturbance frequencies into the flow. The drop-off in mode amplitude towards the higher frequencies is reduced as the duty cycle is lowered and as a result of the duty cycle actuation higher frequencies are automatically introduced. This may explain why the relatively low actuation frequency in the experiments by Bons et al. [1,2] was effective (the nondimensional forcing frequency was 0.843). For $\tau = 0.1$, the amplitude of the fundamental ($n = 1, f = 5$) is $a_1 = 2/(\pi n) \sin \pi n \tau = 0.197$.

When also considering that the wall-normal disturbance component is $\sin 30° = 0.5$ the wall-normal component of the momentum coefficient for the fundamental becomes $0.197 \times 0.5 \times c_\mu = 1.86 \times 10^{-5}$ for $B = 1$ which is roughly an order of magnitude less than the momentum coefficient for the slot forcing. Figure 21 shows that the 2D mode amplitude at $s \approx 0.55C_s$ (slightly downstream of the disturbance input) is indeed an order of magnitude lower for the case with VGJ control when compared with the slot forcing. For $B = 2$, the wall-normal component of the momentum coefficient for the fundamental is $c_\mu = 7.44 \times 10^{-5}$ and of the same order of magnitude as the momentum coefficient of the harmonic slot forcing, $c_\mu = 1.1 \times 10^{-4}$. The lower 2D mode initial amplitude indicates that the 2D disturbance input is more effective for the slot forcing than for the VGJ control with $B = 2$. With VGJ control large $k = 1$ mode amplitudes are obtained shortly downstream of the VGJ location (Fig. 21). Starting near $s \approx 0.6C_s$ the $k = 1$ mode experiences linear growth, slightly less so for the $B = 1$ case. For the uncontrolled flow, the $k = 1$ mode experiences growth starting near $s \approx 0.8C_s$ indicating the onset of transition.

Next, results for the harmonic slot forcing and harmonic VGJ actuation are compared. When considering frequency spectra of the spanwise mode $k = 0$ (2D mode) of the wall-pressure coefficient, c_p, at different downstream locations on the LPT blade (Fig. 23a), the harmonic VGJ actuation is seen to introduce fairly large 2D disturbance amplitudes which for actuation with 3 holes per ΔZ reach the amplitude levels of the slot actuation for $f = 5$. One may extrapolate that when the hole spacing is decreased further the results for the slot forcing are asymptotically approached. In fact, investigations by Gross et al. [9] showed that 2D structures remained the dominant structures for pulsed VGJ actuation and hole spacings between $0.045C_x$ and $0.455C_x$. When comparing Figs. 20a and 23a it can be deduced that harmonic VGJ actuation results in larger disturbance amplitudes for the fundamental ($f = 5$) and its higher harmonic ($f = 10$) than pulsed VGJ actuation despite the lower blowing ratio for the former. This result must, however, be regarded as preliminary as for the present study the frequency of the most amplified 2D mode was known from an a priori study [7]. If the optimal frequency was not known, reduced duty cycle actuation may be advantageous as it introduces a large number of different frequencies (Fig. 22). Chances are that a number of these frequencies lie within the frequency range where 2D disturbances are amplified.

a)   b)
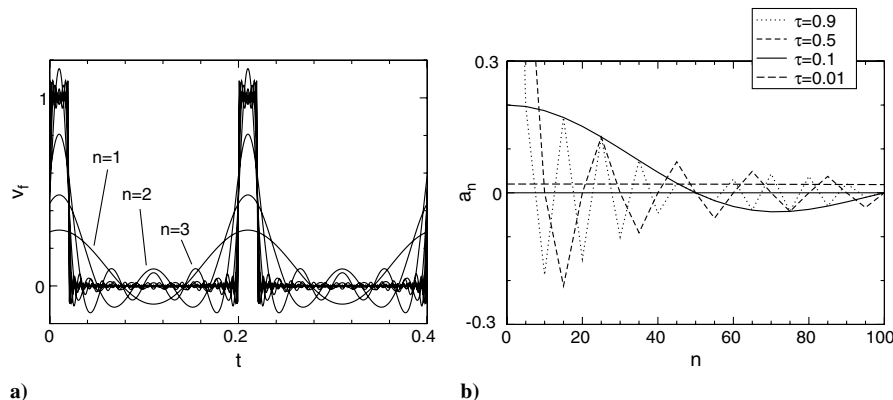
Fig. 22 Graphs of a) reduced duty cycle function for $B = 1$ **and** $\tau = 0.1$ **computed from** $n = 1 \ldots 128$ **Fourier modes, and b) reduced cycle function frequency spectra for** $B = 1$ **and different** τ**.**
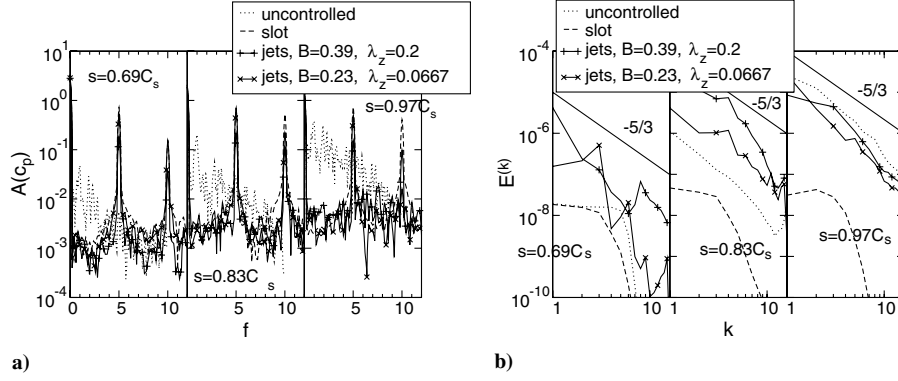
Fig. 23   Graphs of a) frequency spectra of wall-pressure coefficient c_p, and b) estimates of energy spectral density and $-5/3$ slope of inertial subrange.

The energy spectral density distribution estimates at $s = 0.83C_s$ (Fig. 23b) show that for harmonic VGJ actuation the higher spanwise modes ($k > 0$) fill up more quickly than for the uncontrolled flow. At $s = 0.97C_s$ the energy spectra obtained with harmonic VGJ actuation approximately match the spectrum of the uncontrolled flow.

A comparison of the $k = 0$ and $k = 1$ disturbance components of the wall-pressure coefficient for the fundamental $f = 5$ is shown in Fig. 24. Results for the reduced duty cycle actuation were shown in Fig. 21. The 2D ($k = 0$) disturbance amplitude distribution for $\lambda_z = 0.0667$ (3 holes/ΔZ) is very similar to the respective distribution for the slot forcing. Although the momentum coefficient for the slot forcing ($c_\mu = 1.1 \times 10^{-4}$) was smaller than the momentum coefficient for forcing with 3 holes/ΔZ ($c_\mu = 2.2 \times 10^{-4}$) the initial disturbance amplitude near $s = 0.55C_s$ is larger for the slot forcing. However, the $k = 1$ component which is completely suppressed for the slot forcing obtains large amplitude levels for harmonic VGJ actuation, especially for the harmonic forcing with one hole per ΔZ ($\lambda_z = 0.2$). The present simulations suggest that wall-normal injection results in a more effective separation control than angled injection because it results in a larger 2D disturbance component. In fact, Postl also showed this to be the case for low to moderate blowing ratios [10].

4.   POD Analysis

Using the snapshot method [21] we performed a POD [20] of the time-dependent data. We analyzed 40 instantaneous velocity fields (for the entire computational domain) taken at constant intervals in time. For the uncontrolled flow we considered a time interval of 1 (corresponding to the period of the dominant frequency). For the controlled cases we considered time-intervals of 0.2 (corresponding to the period of the actuation).
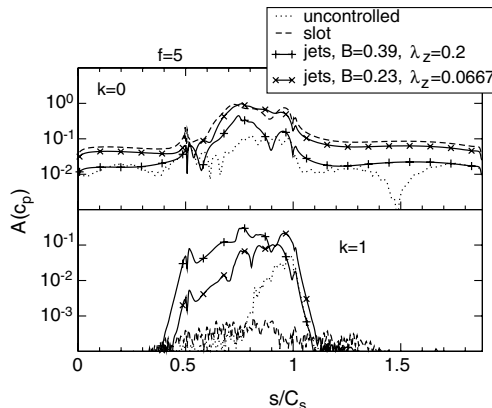
Figure 25 shows the POD eigenvalue spectra. The eigenvalue magnitude is identical to twice the kinetic energy content of the corresponding mode [Eq. (4)]. Modes that appear in pairs with almost equal energy content and eigenfunction distributions that are shifted in downstream direction by $\pi/2$ capture traveling waves. With flow control a larger amount of the kinetic energy of the flow can be captured with less POD modes, indicating that the flow is more regular: the drop-off in mode energy content toward the higher POD modes is more pronounced than for the uncontrolled flow. This is especially true for the case where the flow is controlled by harmonic blowing through a slot. The main difference between the POD eigenvalue spectra for the cases with pulsed VGJ flow control is the higher energy content for modes 1 and 2 for pulsed VGJs with $B = 1$ (compared with $B = 2$) and harmonic VGJs with $B = 0.23$ and $\lambda_z = 0.0667$ (compared with $B = 0.39$ and $\lambda_z = 0.2$). Modes 1 and 2 correspond to spanwise coherent structures that result from the in-phase actuation (in spanwise direction) of the VGJ actuators which introduces a 2D disturbance into the flow that is amplified by the shear layer instability (Figs. 21 and 24).

The most energetic structures have considerable 2D coherence except for pulsed VGJ actuation with $B = 2$ (Fig. 26). For this case, the dominant structures look oblique. With harmonic actuation and 1 hole per ΔZ ($\lambda_z = 0.2$) the dominant coherent structures are initially slightly oblique and near the trailing edge almost perfectly 2D. With 3 holes per ΔZ ($\lambda_z = 0.0667$), structures with large spanwise coherence are obtained that closely resemble those for the slot forcing.

The POD mode time signals are shown in Fig. 27. When considering the uncontrolled flow, the oscillation period of modes 1 and 2 can hardly be determined from the time-signals which appear rather random. From frequency spectra of data taken over a time interval of 20 we determined a period of roughly 1 for the dominant modes which constitute spanwise vortical structures (Fig. 26a) with a
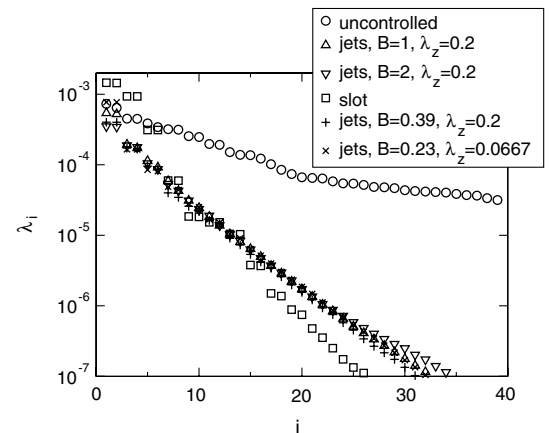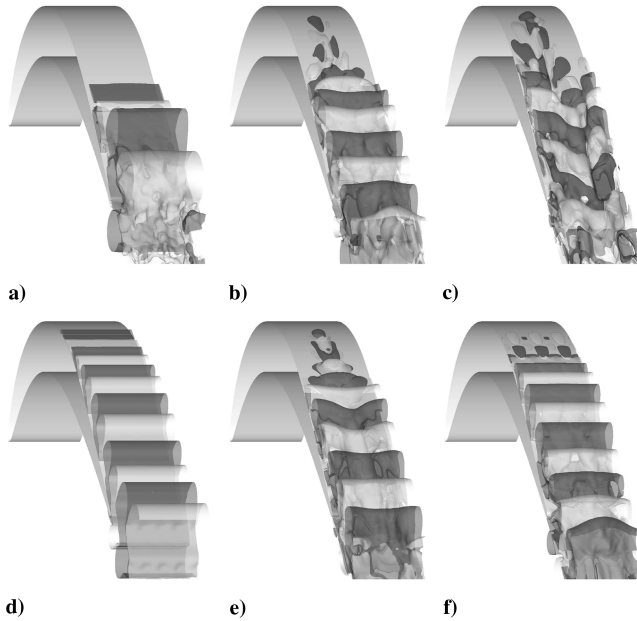

Fig. 24   Amplitude of $f = 5$ disturbance component of spanwise modes $k = 0$ and 1 of wall-pressure coefficient.

Fig. 25   Eigenvalues of POD modes (mode energy content).

Fig. 26 POD mode $i = 1$. **Isosurfaces of** $q_2 = \pm 0.02$: **a) uncontrolled flow. Pulsed VGJs with b)** $B = 1$, **c)** $B = 2$, **and d) harmonic blowing through slot with** $B = 0.1$. **Jets with wall-normal harmonic blowing and e)** $B = 0.390$, $\lambda_z = 0.2$, **and f)** $B = 0.225$, $\lambda_z = 0.0667$.

streamwise wavelength that is longer than for the controlled cases. These low-frequency structures can also be discerned when scrutinizing instantaneous visualizations of the time-dependent data (Fig. 3). As these structures were not artificially introduced into the flow they are likely the result of an instability mechanism of the flow.

With pulsed VGJs for $B = 1$ and with harmonic VGJ actuation for $B = 0.39$ and $B = 0.23$ the dominant structures are also spanwise coherent (Figs. 15 and 26). The period of the corresponding mode 1 and 2 time-signals is 0.2 (Fig. 27) which leads to the conclusion that the spanwise structures are a direct consequence of the actuation. When resorting to Figs. 21 and 24 it can be seen that disturbances with $f = 5$ (which can be associated with the POD modes 1 and 2) are amplified by the flow by roughly 1 order of magnitude. One may argue that for these cases the dominant flow control mechanisms appear to be the earlier transition of the flow and the additional wall-normal mixing facilitated by the spanwise coherent structures which are introduced by the in-phase actuation of the VGJs and which are amplified by the flow. The control is effective and efficient because the disturbances introduced by the actuation are amplified by the flow ("at no cost"). These conclusions were first drawn by Postl [10] based on investigations for a related model problem, separation control for a laminar separation bubble on a flat plate under LPT conditions.

When the amplitude of the reduced duty cycle VGJs is increased to $B = 2$ the time signals of the dominant POD modes are equally

linked to the actuation (the mode 1 and 2 periods are 0.2, Fig. 27). However, compared with $B = 1$ the dominant structures are no longer organized in the spanwise direction but rather oblique (Figs. 15 and 26) resulting in a reduced amplitude of the $k = 0$ Fourier mode for $f = 5$ (Fig. 21). Also, compared with the $B = 1$ case less energy is contained in modes 1 and 2 (Fig. 25). Based on the wall-pressure distributions (Fig. 16a) and the wake velocity profiles (Fig. 18b) we determined that pulsed VGJ actuation is slightly more effective for $B = 2$ than for $B = 1$. However, because actuation with $B = 1$ requires less energy it would be the preferred choice in practical applications.

For pulsed actuation through a slot, modes 1 and 2 up to 15 and 16 (fundamental and higher harmonics) appear in pairs of equal eigenvalue magnitude (Fig. 25) where the mode shape (Fig. 26) and time-coefficients (Fig. 27) belonging to each pair are similar but shifted (in streamwise direction and time, respectively) by a quarter wavelength. Again, the mode 1 and 2 time-signal is directly related to the actuation. When also considering the Fourier amplitudes (Fig. 21) it can be seen that the disturbances (mode $k = 0$, $f = 5$) which are introduced by the actuation are strongly amplified in downstream direction. An effective control is established for very small disturbance inputs and thus at "little cost". Was it not for the harsh turbine operating environment and related doubts about life time limitations and maintenance issues, plasma actuators would certainly be a good choice for introducing such 2D disturbances. When also considering the instantaneous flow visualizations (Fig. 15) and the energy spectral density estimates (Fig. 23b) it appears that transition is delayed. The concept of transition delay at low Reynolds number conditions by spanwise vortices was also investigated by Embacher [15]. It was shown that for a certain frequency range of the spanwise coherent structures the growth rates of secondary instabilities are reduced resulting in a transition delay and relaminarization of an already turbulent flow. This is advantageous as it was found that laminar spanwise vortices facilitate a very effective separation control. In fact, of the various unsteady flow control concepts discussed in this paper separation control by laminar spanwise vortices (slot forcing) was found to be the most effective (Fig. 17).

C. Steady Flow Control-Streamwise Vortices

Instantaneous flow visualizations for the cases with steady flow control are shown in Fig. 28. Although the boundary layer thickness is modulated in the spanwise direction downstream of the forcing location separation, transition, and bubble shedding appear not to be greatly affected for forcing with $A = 1$. For $A = 10$ and $\lambda_z = 0.05$, 0.0667 transition appears delayed compared with the uncontrolled flow (Fig. 3) and high frequency short wavelength spanwise structures (possibly resulting from a secondary instability) are seen to develop on top of the streamwise vortices. These structures were too far away from the wall to imprint a pressure signal on the wall that was large enough to be detected over the background noise. When the wavelength is increased to $\lambda_z = 0.1$ spanwise coherent structures appear near the trailing edge. For $\lambda_z = 0.2$ regions of turbulent flow develop in between the streamwise vortices. Clearly, an optimal
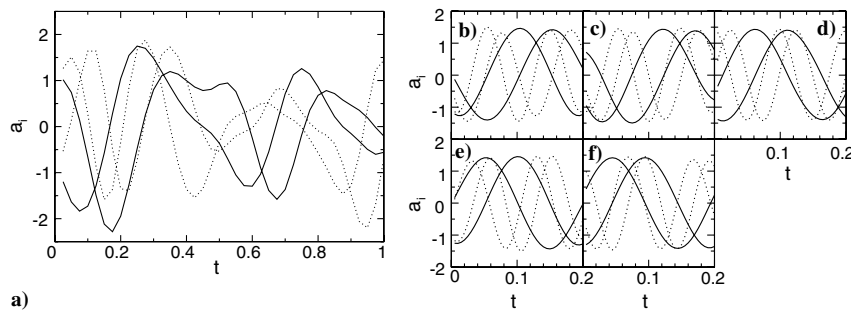
Fig. 27 POD mode time signals a_i. **Solid lines: modes 1 and 2, and dotted lines: modes 3 and 4. Graphs of a) uncontrolled flow, and pulsed VGJs with b)** $B = 1$, **c)** $B = 2$, **and d) harmonic blowing through slot with** $B = 0.1$. **Jets with wall-normal harmonic blowing and e)** $B = 0.390$, $\lambda_z = 0.2$, **and f)** $B = 0.225$, $\lambda_z = 0.0667$.

Fig. 28 Streamwise vortices with spanwise wavelength, $\lambda_z = 0.05$, 0.0667, 0.1, 0.2 (top to bottom), and amplitude $A = 1$ (left) and $A = 10$ (right). Isosurfaces of vortex identification criterion, $Q = 1$, and isocontours of spanwise vorticity, ω_z, at $z = 0$. Computational domain was repeated once in spanwise direction.

spanwise wavelength appears to exist for delaying/suppressing transition with streamwise vortices.

A comparison of the computed wall-pressure distributions is given in Fig. 29a. For $A = 1$ the effect of the streamwise vortices on the flow is minimal (albeit a minute separation delay) and the computed pressure distributions follow the pressure distribution of the uncontrolled flow. The picture changes for $A = 10$. For all 4 cases separation is almost completely eliminated indicated by a strong pressure recovery downstream of $x \approx 0.65$. For $\lambda_z = 0.2$ a slightly less negative c_p is obtained near 65% chord and the c_p-distribution in the pressure recovery region does not follow the curves for $\lambda_z = 0.05$, 0.0667, and 0.1. Isocontours of the streamfunction

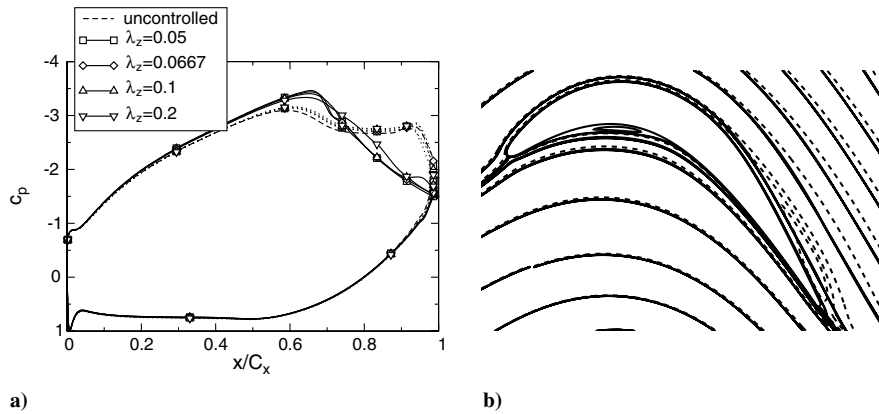a)   b)

Fig. 29   Graphs of a) wall-pressure coefficient (dotted lines: $A = 1$ and solid lines: $A = 10$) and b) isocontours of streamfunction (dashed lines: uncontrolled flow and solid lines: controlled flow, $A = 10$).
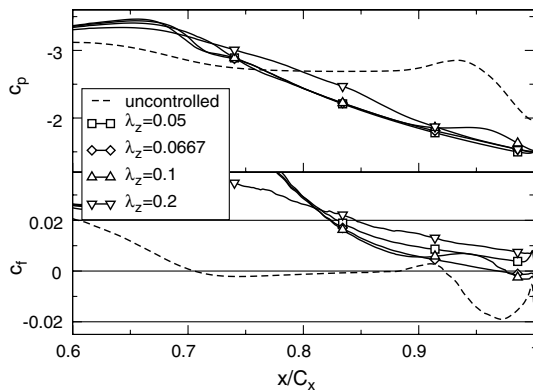

Fig. 30   Wall-pressure coefficient c_p and skin friction coefficient c_f for $A = 10$.
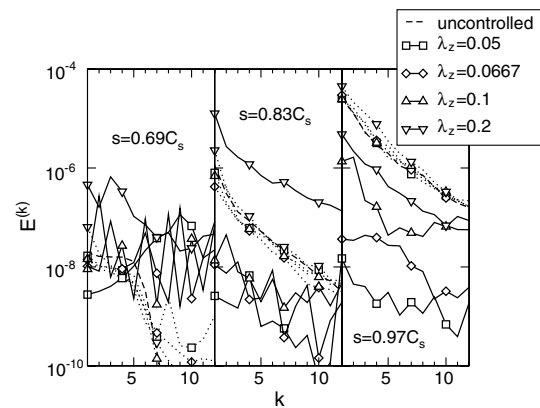

Fig. 32   Estimates of energy spectral density. Dotted lines: $A = 1$ and solid lines: $A = 10$.

(Fig. 29b) indicate fully attached flow on the suction side for $A = 10$. A comparison of the wall pressure and skin friction coefficient for $A = 10$ is shown in Fig. 30. In the mean separation is completely eliminated for $\lambda_z = 0.05$ and $\lambda_z = 0.2$. The appearance of spanwise coherent structures near the trailing edge for $\lambda_z = 0.1$ can be associated with a small "pressure plateau" and a negative skin friction indicating flow separation.

Amplitude distributions of the spanwise modes $k = 1 \ldots 12$ of the time-averaged $(n = 0)$ wall skin friction coefficient, c_f, are compared in Fig. 31. The initial amplitudes near $s \approx 0.6 C_s$ (the streamwise vortices are forced between $x = 0.61 \ldots 0.71$ which corresponds to $s = 0.58 \ldots 0.64$) are about the same in all three instances and 1 order of magnitude larger for $A = 10$ (Fig. 31b) compared with $A = 1$ (Fig. 31a). For $A = 1$ the amplitude of the fundamental (the dominant wavelength introduced by the forcing)

decays quickly and has little effect on the other modes. For $A = 10$ the amplitude of the fundamental still decays independent of the spanwise wavelength. This is not surprising as the boundary layer is convex and, hence, not Görtler-unstable. However, the decay rate near $s \approx 0.8 C_s$ is the smallest for $k = 4$ ($\lambda_z = 0.05$). If the goal was to have strong streamwise vortices near separation then, out of the 4 wavelengths that we investigated, $\lambda_z = 0.05$ would be the preferred choice. When considering the energy spectral density estimates it appears that transition is most successfully delayed for $\lambda_z = 0.05$ (Fig. 32). Unfortunately, as a result of the limited grid resolution in the spanwise direction, flow control by streamwise vortices with even smaller λ_z could not be investigated. Based on the present simulations the conclusion was drawn that for separation control by streamwise vortices the optimal spanwise wavelength is somewhere
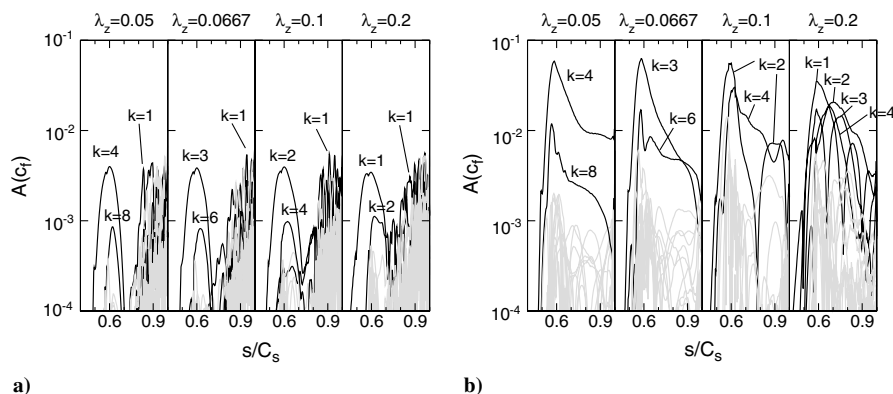

a)   b)

Fig. 31   Amplitudes of spanwise modes, $k = 1 \ldots 12$, of time-averaged skin friction coefficient c_f for a) $A = 1$ and b) $A = 10$. Mode numbers of amplitude distributions drawn in black as indicated. All other mode distributions shown in gray.

Fig. 33 Fine grid solution. Streamwise vortices with spanwise wavelength, $\lambda_z = 0.05$, and amplitude $A = 10$. Isosurfaces of vortex identification criterion, $Q = 1$, and isocontours of spanwise vorticity, ω_z, at $z = 0$. From top to bottom: perspective view of blade, side view of wake, and top down view of wake. Computational domain was repeated once in spanwise direction.

Fig. 35 Amplitudes of spanwise modes k of time-averaged skin friction coefficient c_f. Dashed lines: medium and solid lines: fine grid results for $\lambda_z = 0.05$ and $A = 10$. Shown are modes $k = 1 \ldots 12$.

near or smaller than $\lambda_z = 0.05$. This is not a spanwise wavelength that would be favorable for tripping the flow to turbulence by, e.g., dimples on the surface as our results show that transition is delayed. Also, we are not implying that the present method is a more effective separation control than tripping the flow.

For verification purposes, we repeated the $\lambda_z = 0.05$ and $A = 10$ simulation for the fine grid. An instantaneous flow visualization is shown in Fig. 33. The flow looks qualitatively very similar to the result obtained with the medium resolution grid (Fig. 28). On the fine grid the formation of the high frequency spanwise structures that are situated on top of the streamwise structures is delayed. Wall-pressure coefficient distributions as well as isocontourlines of the streamfunction for the medium and the fine grid are compared in Fig. 34. The pressure distribution for the fine grid is leveling off near the trailing edge indicating incipient flow separation (Fig. 34a). Isocontourlines of the streamfunction also indicate a slight thickening of the suction side boundary layer near the trailing edge (Fig. 34b) which coincides with a lower skin friction coefficient
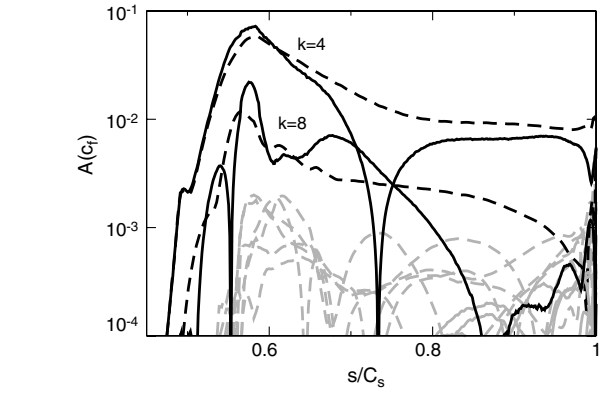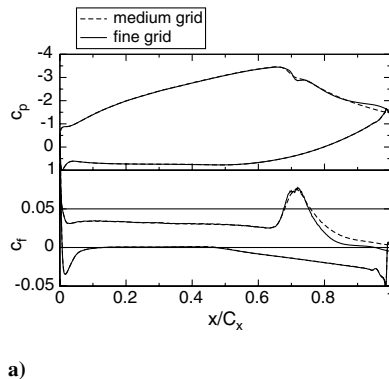
(Fig. 34a). Amplitude distributions of the spanwise modes of the time-averaged skin friction coefficient are compared in Fig. 35. While the amplitude distribution of the fundamental ($k = 4$) for the medium and the fine grid are similar (apart from the deviation near $s = 0.73C_s$) the first higher harmonic ($k = 8$) shows a peak near $s \approx 0.5C_s$ and then decays more quickly for the fine grid. In summary, the concept of transition delay and separation control by streamwise vortices is confirmed by the fine grid results.

V. Conclusions

Laminar separation from LPT blades at low Reynolds number conditions can negatively affect performance. We simulated the flow through a linear LPT cascade using a compressible finite volume Navier–Stokes code. A grid resolution study for the uncontrolled flow showed grid convergence despite the fact that the smallest dissipative scales were not resolved. Apparently, the damping characteristics of the numerical discretization are such that a consistent dissipation of energy is achieved at the high wavenumber end of the spectrum. After the validation of the current approach for the uncontrolled flow we investigated several different separation control approaches: Separation control by pulsed VGJs, by harmonic blowing through a slot (a similar disturbance input could be realized in experiments by plasma actuators), by harmonic wall-normal VGJs, and by steady streamwise vortices (which could in the experiment be realized by, e.g., vortex generators or plasma actuators). With the current parameter settings all approaches were found to successfully reduce or prevent flow separation. The underlying physical mechanisms responsible for the successful separation control and consequently also the effectiveness of the various approaches were, however, found to be different.

With pulsed VGJs and for a blowing ratio of 1, spanwise structures (or rollers) were excited that were amplified by the flow due to

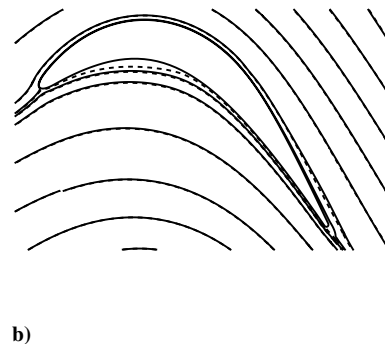a)   b)

Fig. 34 Graphs of a) wall-pressure and skin friction coefficient and b) isocontours of streamfunction for $\lambda_z = 0.05$ and $A = 10$ (dashed lines: medium grid; solid lines: fine grid).

hydrodynamic instability mechanisms. The flow was also seen to transition earlier. Both effects, the earlier transitioning and the spanwise structures embedded in the transitional flow were found to effectively reduce flow separation. The control is efficient because the spanwise structures are amplified by the flow. This amplification requires no external energy input. For the larger blowing ratio of 2, the flow was found to transition even earlier. The embedded spanwise structures were, however, less pronounced and experienced a weaker amplification indicating a less efficient control. Wall-normal harmonic VGJ actuation was found to result in a more effective control at even smaller blowing ratios. This is supported by results by Postl which indicate that for blowing ratios of about 1 wall-normal injection is more effective [10]. Angled injection introduces more streamwise vorticity which promotes earlier transition, which, if spanwise vortices are exploited for separation control, is not beneficial as earlier transition is weakening the spanwise structures. For wall-normal injection, the more closely the VGJ holes are spaced the larger the 2D disturbance that is introduced by the in-phase actuation of the VGJs. This was seen in a simulation where we increased the number of holes in the spanwise direction by 3 while keeping the momentum coefficient constant. For low blowing ratios and wall-normal injection an optimization of the hole spacing and the actuation frequency (reduced duty cycle or alternatively harmonic excitation) such that both, the spanwise structures and transition, are exploited in an optimal fashion for separation control will likely lead to the most effective control.

A surprisingly effective control was accomplished by harmonic blowing through a slot. For a properly chosen forcing frequency, the 2D disturbance input was found to be strongly amplified by the shear layer instability resulting in the formation of laminar spanwise vortices. The growth of 3D disturbances in this time-periodic 2D flow was delayed compared with the uncontrolled flow. The flow was found to transition in the wake downstream of the blade. We speculate that the controlled time-dependent base flow (time average plus 2D structures at forcing frequency $f = 5$) is stable with respect to 3D disturbances up to higher Reynolds numbers than the uncontrolled base flow (time average plus 2D structures at natural shedding frequency, $f \approx 1$).

Because the flow is not centrifugally unstable streamwise vortices are not amplified. Nevertheless, there appears to be an optimum spanwise spacing or wavelength where the streamwise vortices experience the weakest damping. Separation control is accomplished by the wall-normal momentum exchange facilitated by the streamwise vortices. For the same spanwise wavelength streamwise vortices were also found to result in a transition delay which is an added benefit as turbulent mixing would weaken the vortices. Transition was found to be initiated by the appearance of 2D structures with a frequency different from the natural shedding frequency, however. This is in contrast to the transition process for the uncontrolled flow where transition is initiated by the appearance of 3D structures in a flow with strong spanwise structures. In other words, the two mechanisms seem to counteract each other and the suppression of either one of the two may be the foundation for an efficient control.

Spanwise vortices are amplified by the flow but their generation requires external power. Streamwise vortices can be introduced by passive devices such as vortex generators which require no external power but pose a performance penalty at operating conditions where flow separation is not a concern. As the streamwise vortices are not amplified their initial amplitude has to be rather large and the vortex strength that can be achieved with such devices determines their usefulness for separation control. The final choice of a particular flow control technique for a particular application will also be guided by considerations of practicality, associated manufacturing and maintenance expenses, and robustness to varying operating and ambient conditions.

Acknowledgments

References

[1] Bons, J. P., Sondergaard, R., and Rivir, R. B., "Turbine Separation Control Using Pulsed Vortex Generator Jets," *Journal of Turbomachinery*, Vol. 123, No. 2, 2001, pp. 198–206.
doi:10.1115/1.1350410

[2] Bons, J. P., Sondergaard, R., and Rivir, R. B., "The Fluid Dynamics of LPT Blade Separation Control Using Pulsed Jets," *Journal of Turbomachinery*, Vol. 124, No. 1, 2002, pp. 77–85.
doi:10.1115/1.1425392

[3] Sondergaard, R., Bons, J. P., and Rivir, R. B., "Control of Low-Pressure Turbine Separation Using Vortex Generator Jets," *Journal of Propulsion and Power*, Vol. 18, No. 4, 2002, pp. 889–895.
doi:10.2514/2.6014

[4] Rizzetta, D. P., and Visbal, M. R., "Numerical Investigation of Transitional Flow Through a Low-Pressure Turbine Cascade," AIAA Paper AIAA-2003-3587, June 2003.

[5] Rizzetta, D. P., and Visbal, M. R., "Numerical Simulation of Separation Control for Transitional Highly Loaded Low-Pressure Turbines," *AIAA Journal*, Vol. 43, No. 9, 2005, pp. 1958–1967.
doi:10.2514/1.12376

[6] Rizzetta, D. P., and Visbal, M. R., "Numerical Investigation of Plasma-Based Flow Control for a Transitional Highly-Loaded Low-Pressure Turbine," AIAA paper AIAA-2007-938, Jan. 2007.

[7] Gross, A., and Fasel, H. F., "Numerical Investigation of Low-Pressure Turbine Blade Separation Control," *AIAA Journal*, Vol. 43, No. 12, 2005, pp. 2514–2526.
doi:10.2514/1.1013

[8] Gross, A., and Fasel, H. F., "Investigation of Low-Pressure Turbine Separation Control," AIAA Paper AIAA-2007-520, Jan. 2007.

[9] Gross, A., Balzer, W., and Fasel, H. F., "Active Separation Control for Lifting Surfaces at Low-Reynolds Number Operating Conditions," *DoD HPCMP Users Group Conference*, DOI 10.1109/DoD.HPCMP. UGC.2008.23, 2008.

[10] Postl, D., "Numerical Investigation of Laminar Separation Control Using Vortex Generator Jets," Ph.D. Dissertation, Univ. of Arizona, Tucson, AZ, 2005.

[11] Poondru, S., "Large-Eddy Simulation and Active Flow Control of Low-Reynolds Number Flow through a Low-Pressure Turbine Cascade," Ph.D. Dissertation, Univ. of Cincinnati, Cincinnati, OH, 2008.

[12] Abdessemed, N., Sherwin, S. J., and Theofilis, V., "On Unstable 2D Basic States in Low Pressure Turbine Flows at Moderate Reynolds Numbers," AIAA Paper AIAA-2004-2541, June–July 2004.

[13] Abdessemed, N., Sherwin, S. J., and Theofilis, V., "Linear Stability of the Flow Past a Low Pressure Turbine Blade," AIAA Paper AIAA-2006-3530, June 2006.

[14] Huang, J., Corke, T. C., and Thomas, F. O., "Unsteady Plasma Actuators for Separation Control of Low-Pressure Turbine Blades," *AIAA Journal*, Vol. 44, No. 7, 2006, pp. 1477–1487.
doi:10.2514/1.19243

[15] Embacher, M., "Control of Secondary Absolute Instability in Separation Bubbles," Masters Thesis, Univ. of Arizona, Tucson, AZ, 2006.

[16] Fasel, H. F., and Postl, D., "Interaction of Separation and Transition in Boundary Layers: Direct Numerical Simulations," *Sixth IUTAM Symposium on Laminar-Turbulent Transition*, edited by R. Govindarajan, Springer–Verlag, New York, 2006, pp. 71–88.

[17] Cossu, C., and Brandt, L., "Stabilization of Tollmien–Schlichting Waves by Finite Amplitude Optimal Streaks in the Blasius Boundary Layer," *Physics of Fluids*, Vol. 14, No. 8, 2002, pp. 57–60.

[18] Lake, J. P., King, P. I., and Rivir, R. B., "Reduction of Separation Losses on a Turbine Blade With Low Reynolds Number," AIAA Paper AIAA-99-0242, Jan. 1999.

[19] Hansen, L., and Bons, J., "Flow Measurements of Vortex Generator Jets in Separating Boundary Layer," *Journal of Propulsion and Power*, Vol. 22, No. 3, 2006, pp. 558–566.
doi:10.2514/1.13820

[20] Lumley, J. L., "The Structure of Inhomogeneous Turbulent Flows," *Atmospheric Turbulence and Radio Wave Propagation*, edited by A. M. Yaglom and V. I. Tatarsky, Nauka, Moscow, 1967, pp. 166–178.

[21] Sirovich, L., "Turbulence and the Dynamics of Coherent Structures," *Quarterly of Applied Mathematics*, Vol. 45, No. 3, 1987, pp. 561–590.

[22] Gross, A., and Fasel, H. F., "High-Order-Accurate Numerical Method for Complex Flows," *AIAA Journal*, Vol. 46, No. 1, 2008, pp. 204–214.
doi:10.2514/1.22742

[23] Gross, A., and Fasel, H. F., "Characteristic Ghost-Cell Boundary Condition," *AIAA Journal*, Vol. 45, No. 1, 2007, pp. 302–306.
doi:10.2514/1.23130

[24] Hunt, J. C. R., Wray, A. A., and Moin, P., "Eddies, Stream, and Convergence Zones in Turbulent Flows," Center for Turbulence Research, Rept. CTR-S88, Stanford, CA, 1988.

[25] Sohn, K. H., Shyne, R. J., and DeWitt, K. J., "Experimental Investigation of Boundary Layer Behavior in a Simulated Low Pressure Turbine," NASA TM 1998-207921.

[26] Margolin, L. G., and Rider, W. J., "A Rationale for Implicit Turbulence Modeling," *International Journal for Numerical Methods in Fluids*, Vol. 39, No. 9, 2002, pp. 821–841.
doi:10.1002/fld.331

M. Visbal
Associate Editor